D^0 BACKGROUND TO NEUTRINO OSCILLATIONS IN THE OPERA EXPERIMENT

A THESIS SUBMITTED TO
THE GRADUATE SCHOOL OF NATURAL AND APPLIED SCIENCES
OF
MIDDLE EAST TECHNICAL UNIVERSITY

BY

SERHAN TUFANLI

IN PARTIAL FULFILLMENT OF THE REQUIREMENTS
FOR
THE DEGREE OF MASTER OF SCIENCE
IN
PHYSICS

FEBRUARY 2009

Approval of the thesis:

D^0 BACKGROUND TO NEUTRINO OSCILLATIONS IN THE OPERA EXPERIMENT

submitted by **SERHAN TUFANLI** in partial fulfillment of the requirements for the degree of **Master of Science in Physics Department, Middle East Technical University** by,

Prof. Dr. Canan Özgen _____
Dean, Graduate School of **Natural and Applied Sciences**

Prof. Dr. Sinan Bilikmen _____
Head of Department, **Physics**

Assoc. Prof. Dr. Ali Murat Güler _____
Supervisor, **Physics Dept., METU**

Examining Committee Members:

Prof. Dr. Ali Ulvi Yılmazer
Physics Engineering Dept., Ankara University _____

Assoc. Prof. Dr. Ali Murat GÜLER
Physics Dept., METU _____

Prof. Dr. Ramazan Sever
Physics Dept., METU _____

Prof. Dr. Gürsevil Turan
Physics Dept., METU _____

Prof. Dr. Osman Yılmaz
Physics Dept., METU _____

Date: _____

I hereby declare that all information in this document has been obtained and presented in accordance with academic rules and ethical conduct. I also declare that, as required by these rules and conduct, I have fully cited and referenced all material and results that are not original to this work.

Name, Last Name: SERHAN TUFANLI

Signature :

ABSTRACT

D^0 BACKGROUND TO NEUTRINO OSCILLATIONS IN THE OPERA EXPERIMENT

Tufanlı, Serhan
M.S., Department of Physics
Supervisor : Assoc. Prof. Dr. Ali Murat Güler

February 2009, 79 pages

The OPERA experiment is designed to search for ν_τ appearance in almost pure CERN-SPS ν_μ beam. The OPERA detector is placed in the Gran Sasso underground laboratory which is 730 km away from CERN. It is a hybrid set-up which combines a lead/emulsion target with various electronic detectors. The detector is composed of two super modules(SM) which contains about 150,000 ECC bricks. Each of the brick is obtained by stacking 56 lead plates with 57 emulsion films. Behind the each brick, an emulsion film doublet, called Changeable Sheet (CS) is attached in order to confirm tracks produced in neutrino interactions. The CS requires very low background track density in order to ensure the expected performance in the experiment. The background tracks in CS can be erased by a special treatment called as refreshing. A refreshing facility was constructed in the LNGS laboratory. The METU group has participated in the construction of the facility and the production of the CS films from the beginning. The main steps of emulsion refreshing and the test results on emulsion quality after the refreshing will be discussed. A Monte Carlo simulation is performed in order to estimate background to $\nu_\mu \rightarrow \nu_\tau$ oscillation due to D^0 production and decay in the ECC brick. It is found that this background is significant for the short decay path topology of the τ lepton.

Keywords: Neutrino, Neutrino Oscillation, Nuclear Emulsion, Emulsion Refresh, D^0 Background

ÖZ

OPERA DENEYİNDE NEUTRİNO SALINIMLARINA D^0 ARKA FONU

Tufanlı, Serhan
Yüksek Lisans, Fizik Bölümü
Tez Yöneticisi : Doç. Dr. Ali Murat Güler

Şubat 2009, 79 sayfa

OPERA deneyi, yüksek oranda saf CERN-SPS müon nötrino demeti içersinde ν_τ'yu gözlemek amacıyla dizayn edilmiş bir deneydir. OPERA dedektörü CERN'den 730 km uzaklıktaki Gran Sasso yeraltı labaratuvarına(LNGS) kurulmuştur. Dedektör, kurşun/emülsiyon karışımı hedef bölümü ile elektronik dedektörlerin bileşiminden oluşan hibrit yapıya sahiptir. İki süper modülden(SM) oluşmuş dedektörde yaklaşık 150,000 adet tuğla şeklinde dedektör(ECC) vardır. ECC, 56 adet kurşun plaka ile 57 adet emülsiyon filmin birleşiminden oluşmuştur ve 8.3 kg'dır. Her ECC'nin arka yüzüne, oluşan parçacık izlerini doğrulamak amacıyla 2 adet emülsiyon filmden oluşan değiştirilebilir iz ölçücü (CS) eklenmiştir. CS'in verimli bir şekilde çalışabilmesi için, CS üzerindeki arka fon oldukça düşük seviyede tutulmalıdır. Arka fonlar, emülsiyon film yenilenmesi yöntemi ile silinebilirler. Bu amaçla LNGS' e emülsiyon film yenilenme ünitesi kurulmuştur. ODTÜ grubu ünitenin kurulmasından itibaren film yenilenmesine ve CS üretilmesine katkıda bulunmuştur. Bu çalışmada emülsiyon film yenilenmesinin aşamaları ile film yenilenmesinin etkinliği üzerine yapılan testler anlatılacaktır. Ayrıca, $\nu_\mu \rightarrow \nu_\tau$ salınımı için, ECC içinde oluşup bozunan D^0 nun sebep olduğu arka fon Monte Carlo simülasyon yoluyla hesaplanmıştır. Bu simülasyon sonucunda hesaplanan arka fonun, τ leptonunun kısa bozunumları için yüksek olduğu bulundu.

Anahtar Kelimeler: Nötrino, Nötrino Salınımları, Nukleer Emülsiyon, Emülsiyon Tazelenmesi, D^0 Arka Fonu

To Muradiye, Mustafa, Müjgan and Fevziye ...

ACKNOWLEDGMENTS

The work presented in this thesis would not have been possible without the involvement of a number of people. I would like to thank the following persons in particular:

I would like to thank to my supervisor Assoc.Prof. Dr. Ali Murat GÜLER for gave me an opportunity to work in the OPERA experiment. Also I want to thank for everything that he has teached me, for discussions, for helps, for supports and for creative ideas.

A special thank goes to Volkan ÇUHA for his guidance and help. He introduce me to the METU neutrino group and encouraged me everytime.

A special thank also goes to Umut KÖSE for teaching me every details of CS facility processes, and for his friendship.

I would like to thank my group members M.Fatih Bay and Kadir ÖCALAN for their friendship and for his helps. I am very grateful to the CS facility team, especially Akitaka ARIGA for his support, explanations and friendship. Also I want to thank to Alessandra PASTORE and Thomas STRAUSS for their help in MC production for my analysis and for their kindness. Thanks to all the LNGS people that I work together in Gran Sasso.

I would like to thank to INFN for the financial support during the stay in LNGS.

Finally thanks to all of my friends for their endless supports and believe in me.

TABLE OF CONTENTS

LIST OF TABLES

TABLES

LIST OF FIGURES

FIGURES

CHAPTER 1

INTRODUCTION

For what we know today, neutrinos have existed for 15 billion years from the beginning of the universe. The neutrinos come from many different sources: decay of radioactive materials, the Sun, and the Universe. Although neutrinos are abounded in nature, they were first postulated by W. Pauli in 1930[1]. He proposed neutrino to explain the continuous spectrum of β-decay[1]. But it took 20 years to verify its existence experimentally. In 1956 it was first experimentally observed by F. Reines and C. Cowan[2] at Savannah River Nuclear Reactor. F. Reinas was awarded Nobel Prize in 1995 for this discovery. In 1962, M. Lederman, M. Shwartz and J. Steinberger discovered the muon neutrino at Brookhaven National Laboratory(BNL)[3]. For their discovery, they were awarded by Nobel Prize in 1988. The discovery of tau lepton in 1972[4] implied the existence of the third family of neutrino, the tau neutrino. In 2000, the tau neutrino was directly observed by the DONUT[5] collaboration at Fermi National Accelerator Laboratory(FNAL). Based on the LEP experiments, we know that, there are three light neutrinos, ν_e, ν_μ, ν_τ and are paired with their charged leptons: e, μ, τ. Since neutrinos are electrically neutral and do not carry color charge, they only interact through weak interactions. There are two weak interactions: Charged Current(CC) and Neutral Current(NC).

In the Standard Model, neutrinos are defined to be massless. Despite massless of the neutrinos in the theory, several experiments[6, 7, 8] have attempt to measure the mass of neutrinos directly via β-decay, pion decay and tau lepton decay. But there were only successful set of the upper limits,

$$m_{\nu_e} < 2.2eV, \quad m_{\nu_\mu} < 170keV, \quad m_{\nu_\tau} < 15.5MeV. \tag{1.1}$$

The mass of neutrinos is also constraint by cosmological observations which put upper limit

on the sum of neutrino masses,

$$\sum_i m_{\nu_i} \leq 0.42eV. \tag{1.2}$$

Another way to probe the neutrino mass is to search for neutrino oscillation. Neutrino oscillation experiments can be classified as disappearance and appearance experiments. In the disappearance experiment at some distance from the neutrino source of a definite flavor one detects neutrinos of the same flavor. The measured fluxes are compared to measure the disappearance of the original neutrino flavor. In the appearance type experiments, one tries to observe a different flavor than the expected one in a distance L from the source. The OPERA[9] is the only long base line experiment in the appearance mode.

As a short summary, our current knowledge about the neutrino oscillation depends on the parameters,

- Δm^2_{12}, θ_{12} from the solar neutrino experiments
- Δm^2_{23}, θ_{23} from the atmospheric and long base line experiments
- θ_{13}

Historically the first hint for the neutrino oscillation comes from the observation of the Sun neutrinos. The energy of the sun is produced in the thermonuclear reactions in which protons and electrons are converted into helium and electron neutrinos.

$$4p + 2e^- \longrightarrow {}^4He + 2\nu_e + 26.7MeV. \tag{1.3}$$

In 1968 R. Davis and his collaborators measured the flux of these solar neutrinos[10] and they reported that expected flux was significantly lower then the expected value.

For solar neutrinos two kinds of experimental technique are used. The first one is the radiochemical technique(Homestake [11], SAGE [14], GALLEX [12], GNO [13]) and the second one is water-Cherenkov technique(Kamiokande [15], Super-Kamiokande [16], SNO [18]). The main difference between these two types is that while radiochemical experiments can perform integrated measurement of the flux, water-Cherenkov can make real-time measurements which allow us to study energy spectrum, and angular distribution.

- Homestake

  The Homestake experiment started in 1968 and took data until 1996. They used the reaction to detect neutrinos

$$\nu_e + {}^{37}Cl \rightarrow {}^{37}Ar + e^-. \tag{1.4}$$

  The target was 615 tons of perchloro-ethylene (Cl_2Cl_4) that placed 1400 m underground, and it was exposed to the solar neutrinos. As a result of the experiment the ratio between detected and the predicted was [10]

$$\frac{\Phi_{Cl}^{Hom}}{\Phi_{Cl}^{Model}} = 0.34 \pm 0.03 \tag{1.5}$$

- GALLEX/GNO and SAGE

  In these experiments detection was performed based on the reaction

$$\nu_e + {}^{71}Ga \rightarrow {}^{71}Ge + e^-. \tag{1.6}$$

  According to the detection results GALLEX/GNO detected $74.1^{+5.4+4.0}_{-5.4-4.2}$, SAGE detected $70.8^{+5.3+3.7}_{-5.2-3.2}$ whereas the expected number of events were 128^{+9}_{-7}.

- Kamiokande and Super-Kamiokande

  Kamiokande was the first water-Cherenkov detector. It was 3000 tons of pure water that placed 1000m underground in Kamioke mine in Japan. It started to work in 1984 and continued until 1995. After that, it was upgraded to 50 kton of pure water, it is named Super-Kamiokande experiment. Water is inside an huge tank that has 11146 PMTs on the inner surface and 1185 PMTs surrounds the outer surface of the tank. In both Kamiokande and Super-Kamiokande neutrinos are observed according to detection of the Cherenkov rings that is produced by electrons emitted in the elastic process.

$$\nu_x + e^- \rightarrow \nu_x + e^- \quad x = e, \mu, \tau. \tag{1.7}$$

  As the final results of the Kamiokande and Super-Kamiokande the ratio between expected and detected flux of the solar neutrinos is

$$\frac{\Phi^{SK}}{\Phi^{Model}} = 0.465 \pm 0.015. \tag{1.8}$$

- SNO

Recently strong model independent evidence in flavor of the transition of the solar ν_e into ν_μ and ν_τ was obtained in the SNO experiment. The detector in the SNO experiment is a heavy water Cherenkov detector-1 kton of D_2O. Neutrinos from the sun are detected via the observation of the following three reactions:

1. CC reaction

$$\nu_e + d \longrightarrow e^- + p + p, \tag{1.9}$$

2. NC reaction

$$\nu_x + d \longrightarrow \nu_x + n + p, \tag{1.10}$$

3. ES process

$$\nu_x + e \longrightarrow \nu_x + e \tag{1.11}$$

From the observation of the solar neutrinos through the detection of the CC and NC reactions for the total fluxes of ν_e and ν_e, ν_μ, ν_τ it was found, respectively

$$\Phi_{\nu_e}^{SNO} = (1.68 \pm 0.06).10^6 cm^{-2} s^{-1} \tag{1.12}$$

and

$$\Phi_{\nu_{e,\mu,\tau}}^{SNO} = (4.94 \pm 0.21).10^6 cm^{-2} s{-}1. \tag{1.13}$$

Thus the total flux of ν_e,ν_μ and ν_τ is about three times larger than the flux of ν_e. As a result ν_e disappearance was detected.

By combining all measurements, Δm_{12}^2(solar mass square difference), $sin^2(\theta_{12})$(and solar mixing angle) are found to be,

$$\Delta m_{12}^2 = 7.1^{+0.5}_{-0.5} \times 10^{-5}\ eV^2, \tag{1.14}$$

and

$$sin^2(\theta_{12}) = 0.30^{+0.09}_{-0.04} \quad \theta_{12} = 32.5^0. \tag{1.15}$$

Atmospheric neutrinos are produced mainly in the decays of secondary particles ($\pi^\pm$, $\mu^\pm$) that created in the interaction of cosmic rays with the atmosphere.

$$\pi^\pm \longrightarrow \mu^\pm + \nu_\mu(\bar{\nu_\mu}) \ , \ \mu^\pm \longrightarrow e^\pm + \nu_\mu(\bar{\nu_\mu}) + \nu_e(\bar{\nu_e}). \tag{1.16}$$

We know that, the flux of cosmic rays that lead to neutrinos with energies above a few GeV is isotropic. So that these neutrinos are produced at the same rate all around the Earth. This

means that neutrino upward-going and downward-going fluxes must be equal. If there is no any effect (like oscillation) on neutrinos, for the number of the electron (muon) events we have the following relation

$$N_l(\cos\theta_z) = N_l(-\cos\theta_z) \tag{1.17}$$

where θ_z is the zenith angle. But from the experiments MACRO [19], SuperKamiokande [20], Soudan2 [21] significant violation of the zenith angle relation is observed. This situation is known as the *atmospheric neutrino anomaly*. And this anomaly can be explained by the assumption of $\nu_\mu \rightarrow \nu_\tau$ oscillation.

- MACRO Experiment

  The analysis of MACRO experiment showed an anomalous zenith angle distribution and a deficit of the total number of upgoing muons. The ν_μ was detected via charged current interactions by the help of streamer tubes and scintillator planes. The results were the confirmation of $\nu_\mu \rightarrow \nu_\tau$ oscillation. MACRO obtained global fit to $\Delta m^2_{23} = 2.3 \times 10^{-3}\ eV^2$ and to $sin^2 2\theta_{23} \sim 1$.

- SuperKamiokande

  The most important support to $\nu_\mu \rightarrow \nu_\tau$ oscillation explanation of atmospheric neutrino anomaly came from the SuperKamiokande experiment. In 1998, the SuperKamiokande collaboration announced evidence for neutrino oscillation in the atmospheric neutrino flux. There was a strong discrepancy in the zenith angle distribution with respect to no oscillation case.

  $$R = 0.658 \pm 0.016 \pm 0.032 \ \ (SuperKamiokande(sub-GeV))$$
  $$R = 0.702 \pm 0.031 \pm 0.099 \ \ (SuperKamiokande(multi-GeV)).$$

  As a result for the values $1.4 \times 10^{-3} < \Delta m^2_{23} < 3.7 \times 10^{-3}$, $sin^2 2\theta_{23} > 0.92$, neutrino oscillation is the most reasonable explanation of the atmospheric neutrino anomaly.

- Soudan2

  Soudan2 is an fine-grained iron calorimeter that is placed Soudan mine, Minnesota, USA. The main results were obtained from the analysis of the fully contained events coming mostly from quasi-elastic neutrino interactions. According to its results, neutrino oscillation scenario that is found by SuperKamiokande is confirmed in Soudan2 experiment. They found the ratio $R = 0.69 \pm 0.12$.

Accelerators supply artificial neutrino source to study neutrino oscillation in the atmospheric region. In accelerator experiments both neutrino energy E and distance between neutrino source and detector, L, can be optimized for the maximum oscillation probability. K2K and MINOS are examples of such experiments.

- K2K

  K2K [22] (KEK to Kamioka) in Japan, is ν_μ beam that is produced by 12 GeV proton beam in KEK accelarator and directed to the SuperKamiokande detector. There is 250 km between the KEK and SuperKamiokande and average energy of the neutrino is 1.3 GeV. There is also another small detector in the KEK that measures the flux of the produced ν_μ. Therefore by comparing the flux of neutrinos in the KEK and SuperKamiokande they get an idea about the oscillation. The results that K2K collaboration presented in 2006 [23], $sin^2 2\theta_{23} = 1$, $1.8 \times 10{-}3eV^2 < \Delta m^2_{23} < 3.6 \times 10^{-3} eV^2$ has a good agreement to the oscillation parameters expected in atmospheric region.

- NuMi

  NuMi-MINOS [24] experiment is similar to K2K. The ν_μ beam is produced in Fermilab and sent to the 735 km far Soudan mine where the detector is placed. There is two identical detector in the MINOS experiment. The near detector is placed 1 km away to the source and it is composed of calorimeters. The far detector has the same structure but it is bigger than the near detector. The far detector is 5.4 kton mass to create target and 1.2 Tesla magnetic field to discriminate neutrinos, anti-neutrinos and CC, NC interaction.

  According to the first results of this experiment 92 events have been observed that has 5σ deficit with respect to the the number of events expected in absence of oscillations, 177 ± 11. The parameters that measured in the experiment is as follows, $sin^2 2\theta_{23} = 1$, $\Delta m^2_{23} = 2.74 \times 10^{-3} eV^2$.

Although there are many experimental evidences of neutrino oscillation in atmospheric region as described above, all of them are disappearance type experiments. Still the direct observation of oscillation in atmospheric region, i.e appearance of $\nu_\mu \rightarrow \nu_\tau$, is missing. In that context the OPERA experiment at Gran-Sasso in Italy was constructed to search for the direct observation of ν_τ in almost pure CNGS ν_μ beam[9].

The thesis is organized as follows: in the next chapte, a theoretical overview on neutrino mass and neutrino oscillation will be given. In Chapter 3, the OPERA experiment will be described in details. In Chapter 4, the properties of the OPERA emulsions and the tests results on the quality of emulsions will be given. In Chapter 5, refreshing process of the CS emulsions and its efficiency will be considered. In Chapter 6, a Monte Carlo study on D^0 charm background to neutrino oscillation in the OPERA experiment will be presented.

CHAPTER 2

THEORY OF NEUTRINO OSCILLATION

In the Standard Model, neutrinos are introduced as massless. However, there is no fundamental reason why the neutrinos should be massless. It would be more natural for them to have finite masses, like all other fermions. In fact most extensions of the Standard Model predicts massive neutrinos. In the following sections, we will see that how the mass rise in the theory.

2.1 Massive Neutrinos: Dirac vs. Majorana

All fundamental fermions obey the Dirac equations and are described by four component spinors, since all have both helicity states. As massive fermions, neutrinos should be described by the same type of four component fermions. However, the difference between neutrinos and other fundamental fermions is that, neutrinos are electrically neutral so the only global quantum number they can carry is the lepton number. If the total lepton number is conserved, the mechanism for neutrino masses is essentially equivalent to the mechanism that provide mass for quarks and leptons. This implies that neutrino would be a Dirac particles. If the lepton number is violated, it would be an indication that neutrinos are Majorana particles. In the following section, we will discussed both Dirac and Majorana neutrinos.

2.1.1 Dirac Neutrinos and Dirac Mass

In the extensions of the Standard Model, one can introduce extra fermions so that model can predict massive neutrinos. If the neutrinos were massless, they could be described by two component complex spinors, called Welly spinors. On the other hand, if we consider the massive neutrinos, its states can be described by four-spinors like all other fermions. Two of

these states are defined as left and right helicity states $\nu_L,\ \nu_R$, and other two helicity states of its anti-particle $\bar{\nu}_L,\ \bar{\nu}_R$. These four spinors are described by the Dirac Lagrangian,

$$\mathcal{L} = \bar{\nu}(i\gamma.\partial - m)\nu \tag{2.1}$$

where $\bar{\nu}$ and ν are the neutrino fields and m is the mass of neutrino. By using Euler-Lagrange equation,

$$\partial_\mu(\frac{\partial L}{\partial(\partial_\mu \nu)}) - \frac{\partial L}{\partial \nu} = 0, \tag{2.2}$$

$$(\frac{\partial L}{\partial(\partial_\mu \nu)}) = \bar{\nu} i\gamma \Rightarrow \partial_\mu(\bar{\nu} i\gamma) = 0. \tag{2.3}$$

$$\frac{\partial L}{\partial \nu} = \bar{\nu}(i\gamma.\partial - m). \tag{2.4}$$

One can obtain the equations of motions as,

$$(i\gamma.\partial - m)\bar{\nu} = 0 \tag{2.5}$$

and

$$(i\gamma.\partial - m)\nu = 0. \tag{2.6}$$

where γ_μ's are the Dirac matrices: $\gamma_0,\ \gamma_1,\ \gamma_2,\ \gamma_3$ and γ_5

$$\vec{\gamma} = \begin{pmatrix} 0 & \vec{\sigma} \\ -\vec{\sigma} & 0 \end{pmatrix}, \gamma_0 = \begin{pmatrix} 1 & 0 \\ 0 & -1 \end{pmatrix}, \gamma_5 = \begin{pmatrix} 0 & 1 \\ 1 & 0 \end{pmatrix} \tag{2.7}$$

$$\gamma_5 = \gamma_0\gamma_1\gamma_2\gamma_3 \tag{2.8}$$

and they have the following properties,

$$\gamma_5^2 = 1, \quad [\gamma_5, \gamma_\mu] = 0. \tag{2.9}$$

Now, let's define the four-component Dirac spinors as $u(\vec{p}, s)$ and $v(\vec{p}, s)$ which are the solutions of the Dirac equation,

$$(\gamma.p - m)u(\vec{p}, s) = 0, \tag{2.10}$$

and

$$(\gamma.p + m)v(\vec{p}, s) = 0\ . \tag{2.11}$$

By using the completeness relation, one gets

$$\sum_{s=1,2} u_p^s \bar{u}_p^s = p + m, \ \ and \ \ \sum_{s=1,2} v_p^s \bar{v}_p^s = p - m \tag{2.12}$$

where

$$p = \gamma^{\mu} p_{\mu}, \tag{2.13}$$

$$\bar{u} = u^{\dagger}\gamma^{0}. \tag{2.14}$$

After the normalization we obtain the four spinor field of neutrino as [25],

$$u(\vec{p}, s) = \sqrt{\frac{E+m}{2m}} \begin{pmatrix} 1 \\ \frac{\vec{\sigma}.\vec{p}}{E+m} \end{pmatrix} \mathcal{X}_s, \tag{2.15}$$

$$v(\vec{p}, s) = \sqrt{\frac{E+m}{2m}} \begin{pmatrix} \frac{\vec{\sigma}.\vec{p}}{E+m} \\ 1 \end{pmatrix} \bar{\mathcal{X}}_s \tag{2.16}$$

with

$$\mathcal{X}_s = \begin{pmatrix} 1 \\ 0 \end{pmatrix} \; for \;\; s = +\frac{1}{2}, \;\; \begin{pmatrix} 0 \\ 1 \end{pmatrix} \; for \;\; s = -\frac{1}{2}, \tag{2.17}$$

$$\bar{\mathcal{X}}_s = -\begin{pmatrix} 0 \\ 1 \end{pmatrix} \; for \;\; s = +\frac{1}{2}, \;\; \begin{pmatrix} 1 \\ 0 \end{pmatrix} \; for \;\; s = -\frac{1}{2}. \tag{2.18}$$

After finding the four spinors lets discuss the mass of the dirac neutrinos. The mass term in the Dirac Lagrangian is

$$-m\bar{\nu}\nu. \tag{2.19}$$

Each field can be represented as a sum of two different helicities: $\nu = \nu_L + \nu_R$. The projection operators are defined as follows,

$$P_R = \frac{1+\gamma_5}{2} \quad , \quad P_L = \frac{1-\gamma_5}{2}, \tag{2.20}$$

which, when they applied to the ν fields, give

$$\nu_R = P_R \nu \quad , \quad \nu_L = P_L \nu. \tag{2.21}$$

When they are substituted to the Lagrangian we obtain,

$$\mathcal{L}_{mass} \sim -m[(\bar{\nu}_R + \bar{\nu}_L)(\nu_R + \nu_L)] \tag{2.22}$$

$$= -m(\bar{\nu}_L \nu_R + \bar{\nu}_R \nu_L + \bar{\nu}_L \nu_L + \bar{\nu}_R \nu_R), \tag{2.23}$$

where the last two terms vanish and finally we obtain mass term as

$$\mathcal{L}_{mass} \sim -m(\bar{\nu}_L \nu_R + \bar{\nu}_R \nu_L). \tag{2.24}$$

In order to have massive neutrinos in the Dirac Lagrangian, there must be both left and right handed neutrinos in the nature. But it was shown by M. Goldhaber et.al [26] that there exists only left-handed neutrinos and right-handed anti-neutrinos in the nature. This implies that the mass term in the Dirac Lagrangian will vanish. On the other hand if neutrinos are massive they are not Dirac particles.

The description of neutrino mixing starts with relationship between weak(or flavor) and mass eigenfields(and states) which arise when more than one-generation of neutrinos is present. The mixed neutrino flavor lead to a mass matrix in the mass Lagrangian as

$$\mathcal{L} \sim -\bar{\nu} M \nu, \tag{2.25}$$

where M is a NxN matrix. If left and right-handed fields are applied to this mass term one gets

$$\mathcal{L} \sim -(\bar{\nu}_R M \nu_L + \bar{\nu}_L M \nu_R), \tag{2.26}$$

where

$$\nu_L = \begin{pmatrix} \nu_e \\ \nu_\mu \\ \nu_\tau \end{pmatrix}, \nu_R = \begin{pmatrix} \nu_e \\ \nu_\mu \\ \nu_\tau \end{pmatrix}. \tag{2.27}$$

Since $MM^\dagger$ is a hermitian its eigenvalues are always positive. Therefore we can say that there exists a unitary matrix U such that

$$MM^\dagger = U m_d^2 U^\dagger \tag{2.28}$$

where

$$m_d^2 = \begin{pmatrix} m_1^2 & 0 & 0 \\ 0 & m_2^2 & 0 \\ 0 & 0 & m_3^2 \end{pmatrix}. \tag{2.29}$$

The diagonalization of the mass matrix implies, there exists another unitary matrix V such that

$$M = U m_d V^\dagger, \tag{2.30}$$

or

$$m_d = U^\dagger M V, \tag{2.31}$$

where

$$m_d = \begin{pmatrix} m_1 & 0 & 0 \\ 0 & m_2 & 0 \\ 0 & 0 & m_3 \end{pmatrix}. \tag{2.32}$$

From Eqn.(2.31) we have

$$V^{\dagger} = m_d^{-1} U^{\dagger} M \tag{2.33}$$

so that

$$VV^{\dagger} = (m_d^{-1} U^{\dagger} M)(M^{-1} U m_d) = 1 \tag{2.34}$$

which shows V is a unitary matrix. So as a result the flavor states ν_L and ν_R are related to the mass eigenfields N_L and N_R through

$$\nu_L = UN_L, \nu_R = VN_R, \tag{2.35}$$

where

$$N_{L,R} = \begin{pmatrix} \nu_1 \\ \nu_2 \\ \nu_3 \end{pmatrix}_{L,R} . \tag{2.36}$$

If we substitute this result into the Eqn. 2.26 we get

$$\mathcal{L}_{mass} = -\bar{N}_L U^{\dagger} M V \bar{N}_R = -\bar{N}_L m_d N_R = -\sum_k m_k \bar{\nu_{k,L}} \nu_{k,R}. \tag{2.37}$$

2.1.2 Majorana Neutrinos and Majorana Mass

In 1937, Majorana showed that a massive neutral fermion can be described by a spinor with only two independent components. Since neutrino is a neutral particle it can be described by a two component spinors that is it has own anti-particle. The free Lagrangian that describes Majorana mass term is given by,

$$\mathcal{L}_{mass} = -\frac{1}{2} \bar{\nu}_L^C \mathcal{M} \nu_L + h.c. \tag{2.38}$$

where $\mathcal{M}$ is complex 3x3 mass matrix, and

$$\nu_L = \begin{pmatrix} \nu_e \\ \nu_\mu \\ \nu_\tau \end{pmatrix}_L . \tag{2.39}$$

Here

$$\nu_L^C = C\bar{\nu}_L^T; \quad \bar{\nu}_L^C = -\nu_L^T C^{-1}, \tag{2.40}$$

where C is the charge conjugation matrix which satisfies the following conditions

$$C\gamma_\alpha^T C^{-1} = -\gamma_\alpha, C^T = -C. \tag{2.41}$$

In Majorana case one can show that

$$\bar{\nu}_L^C \mathcal{M} \nu_L = \nu_L^T (C^{-1})^T \mathcal{M}^T \nu_L = \bar{\nu}_L^C \mathcal{M}^T \nu_L. \tag{2.42}$$

Therefore, the Majorana mass matrix is symmetric:

$$\mathcal{M} = \mathcal{M}^T. \tag{2.43}$$

$\mathcal{M}$ can be diagonalized by using a unitary matrix $\mathcal{U}$ as

$$\mathcal{U}^T \mathcal{M} \mathcal{U} = m_D.$$

By introducing mass eigenfield N_L,

$$\nu_L = \mathcal{U} N_L, \tag{2.44}$$

and substituting into Eqn. 2.38, one can obtain the Majorana mass Lagrangian as

$$\mathcal{L}_{mass}^M = -\frac{1}{2}[\bar{N}_L^C m_D N_L + \bar{N}_L m_D N_L^C]. \tag{2.45}$$

By defining the Majorana field,

$$\nu_M \equiv N_L + N_L^C, \tag{2.46}$$

Eqn. 2.45 can be written as

$$\mathcal{L}_{mass}^M = -\frac{1}{2}\bar{\nu}_M m_D \nu_M = -\frac{1}{2}\sum_k m_k \bar{\nu}_{M,k} \nu_{M,k}. \tag{2.47}$$

As an example, let us consider the following mass Lagrangian,

$$\mathcal{L}_{mass} = -\frac{1}{2}\bar{\nu}_L^C \mathcal{M} \nu_L + h.c., \tag{2.48}$$

where

$$\nu_L = \begin{pmatrix} \nu_e \\ \\ \nu_\mu \end{pmatrix}_L,$$

and

$$\mathcal{M} = \begin{pmatrix} m_{ee} & m_{e\mu} \\ \\ m_{e\mu} & m_{\mu\mu} \end{pmatrix}. \tag{2.49}$$

By diagonalizing matrix $\mathcal{M}$, one can find the following eigenvalues:

$$m_1^{'} = \frac{m_{ee} + m_{\mu\mu}}{2} - \frac{1}{2}\sqrt{4m_{e\mu}^2 + (m_{\mu\mu} - m_{ee})^2}, \tag{2.50}$$

$$m_2^{'} = \frac{m_{ee} + m_{\mu\mu}}{2} + \frac{1}{2}\sqrt{4m_{e\mu}^2 + (m_{\mu\mu} - m_{ee})^2}. \tag{2.51}$$

Since $\mathcal{M}$ is real and symmetric, there exists a unitary matrix O which diagonalizes $\mathcal{M}$ as,

$$O^T \mathcal{M} O = m_D \;\; or \;\; \mathcal{M} = O m_D O^T, \tag{2.52}$$

where

$$m_D = \begin{pmatrix} m_1^{'} & 0 \\ 0 & m_2^{'} \end{pmatrix}, \tag{2.53}$$

and

$$O = \begin{pmatrix} \cos\theta & \sin\theta \\ -\sin\theta & \cos\theta \end{pmatrix}. \tag{2.54}$$

Here θ, mixing parameter, is given by

$$\tan 2\theta = \frac{2m_{e\mu}}{m_{\mu\mu} - m_{ee}}, \tag{2.55}$$

or

$$\sin 2\theta = \frac{2m_{e\mu}}{[4m_{e\mu}^2 + (m_{\mu\mu} - m_{ee})^2]^{\frac{1}{2}}}. \tag{2.56}$$

Although the eigenvalue $m_i^{'}$ can be negative or positive, the physical mass must be positive. In order to obtain definite mass one introduces $\eta_i = \pm 1$ such that

$$m_i^{'} = |m_i^{'}|\eta_i \equiv m_i \eta_i, \tag{2.57}$$

and

$$m_D = \begin{pmatrix} m_1\eta_1 & 0 \\ 0 & m_2\eta_2 \end{pmatrix}. \tag{2.58}$$

Using Eqn. 2.44, the mass term in the Lagrangian can be written as,

$$\mathcal{L}_{mass} = -\frac{1}{2}(\bar{N}_L^C m_D N_L), \tag{2.59}$$

$$= -\frac{1}{2}\sum_k m_k \bar{\chi}_k \chi_k \tag{2.60}$$

where

$$\chi_k = N_{L,k} + \eta_k N_{L,k}^C \tag{2.61}$$

is the Majorana field with definite mass and charge conjugation phase η_k. By using Eqn. 2.44 and Eqn. 2.61 we obtain

$$\chi_1 = \cos\theta \nu_{e,L} - \sin\theta \nu_{\mu,L} - (\cos\theta \nu_{e,L}^C - \sin\theta \nu_{\mu,L}^C), \tag{2.62}$$

$$\chi_2 = \sin\theta\nu_{e,L} + \cos\theta\nu_{\mu,L} + (\sin\theta\nu^C_{e,L} + \cos\theta\nu^C_{\mu,L}) \tag{2.63}$$

or

$$\chi_{1,L} = \cos\theta\nu_{e,L} - \sin\theta\nu_{\mu,L}, \tag{2.64}$$

$$\chi_{2,L} = \sin\theta\nu_{e,L} + \cos\theta\nu_{\mu,L}, \tag{2.65}$$

or

$$\nu_{e,L} = \cos\theta\chi_{1,L} + \sin\theta\chi_{2,L}, \tag{2.66}$$

$$\nu_{\mu,L} = -\sin\theta\chi_{1,L} + \cos\theta\chi_{2,L}. \tag{2.67}$$

2.1.3 Dirac-Majorana Mixing

Up to now, Dirac and Majorana mass terms were discussed separately. On the other hand, both Majorana and Dirac terms can be added. Then the total Majorana and Dirac mass term in the Lagrangian is

$$\mathcal{L}^{D-M}_{mass} = -M_D\bar{\nu}_L\nu_R - \frac{1}{2}(m_L\bar{\nu}^C_L\nu_L + m_R\bar{\nu}^C_R\nu_R) \tag{2.68}$$

where M_D is Dirac mass and m_L, m_R are Majorana masses. Neutrino field is defined as

$$\nu \equiv \begin{pmatrix} \nu_L \\ \nu^C_R \end{pmatrix}. \tag{2.69}$$

Then Eqn. 2.68 can be written as

$$\mathcal{L}^{D-M}_{mass} = -\frac{1}{2}\bar{\nu}^C\mathcal{M}\nu + h.c, \tag{2.70}$$

where

$$\mathcal{M} = \begin{pmatrix} m_L & M_D \\ M_D & m_R \end{pmatrix}. \tag{2.71}$$

Since the mass matrix is similar to the Majorana case, one can follow similar approach to find the eigenvalues. But lets use another way and describe $\mathcal{M}$ in the form

$$\mathcal{M} = \frac{1}{2}Tr\mathcal{M} + \underline{M}, \tag{2.72}$$

where $Tr\mathcal{M} = m_L + m_R$ and

$$\underline{M} = \begin{pmatrix} -\frac{1}{2}(m_R - m_L) & M_D \\ M_D & \frac{1}{2}(m_R - m_L) \end{pmatrix}. \tag{2.73}$$

For the symmetric real matrix one has

$$\underline{M} = O\underline{m}O^T, \tag{2.74}$$

where

$$O = \begin{pmatrix} \cos\theta & \sin\theta \\ -\sin\theta & \cos\theta \end{pmatrix}. \tag{2.75}$$

Finally, eigenvalues of the matrix $\underline{M}$ can be found as,

$$\underline{m}_{1,2} = \pm\frac{1}{2}\sqrt{(m_R - m_L)^2 + 4M_D}. \tag{2.76}$$

Therefore, combining equations 2.74, 2.75, 2.76 one can find expressions for $\sin 2\theta$ and $\tan 2\theta$ as

$$\cos 2\theta = \frac{m_R - m_L}{\sqrt{(m_R - m_L)^2 + 4M_D^2}}, \quad \tan 2\theta = \frac{2M_D}{m_R - m_L}. \tag{2.77}$$

Then, so if we turn back to the relation for $\mathcal{M}$,again by using

$$\mathcal{M} = Om^{'}O^T \tag{2.78}$$

one can find the general eigenvalues for $\mathcal{M}$ as

$$m^{'}_{1,2} = \frac{1}{2}(m_R + m_L) \pm \sqrt{(m_R - m_L)^2 + 4M_D^2}. \tag{2.79}$$

The eigenvalues $m^{'}_i$ can be both positive and negative. So by using

$$\mathcal{L}^{L-D}_{mass} = -\frac{1}{2}\bar{\nu}^C\mathcal{M}\nu + h.c. \tag{2.80}$$

and

$$\nu \equiv \begin{pmatrix} \nu_L \\ \nu^C_R \end{pmatrix} \tag{2.81}$$

one obtains,

$$\nu_L = \cos\theta\nu_1 + \sin\theta\nu_2, \tag{2.82}$$

$$\nu^C_R = -\sin\theta\nu_1 + \cos\theta\nu_2, \tag{2.83}$$

or

$$\nu_1 = \cos\theta\nu_L - \sin\theta\nu^c_R, \tag{2.84}$$

$$\nu_2 = \sin\theta\nu_L + \cos\theta\nu^c_R. \tag{2.85}$$

Now let's consider special case where $m_R \gg M_D, m_L$. By setting $m_L = 0$ one finds

$$m_1 \simeq \frac{M_D}{m_R}, m_2 \simeq m_R. \tag{2.86}$$

Furthermore, the mixing angle θ approaches zero so ν_L and ν_R are completely decoupled. This mechanism is called as seesaw and it explains the smallness of the neutrino mass.

2.2 Neutrino Oscillation

Over the past ten years, an astonishing sequence of experimental results have revealed, without a doubt, that neutrinos change flavor. This means that a neutrino produced in a well-defined weak eigenstate ν_α can be detected in a distinct weak eigenstate ν_β after propagating a macroscopic distance. Furthermore it has been established that the rate of flavor change $P_{\alpha\beta}$ depends on the neutrino energy E_ν and on the propagation distance L.

The simplest and completely satisfactory way to explain the observed neutrino flavor changing phenomena is to postulate that neutrinos have distinct, nonzero masses, and the neutrino mass eigenstates are different from the neutrino weak eigenstates. So, neutrino will undergo neutrino oscillation as they propagate, and $P_{\alpha\beta}$ will be the oscillation probability. Besides L and E_ν, $P_{\alpha\beta}$ is a function of neutrino mass-squared differences $\Delta m^2_{ij} \equiv m^2_j - m^2_i$. In the weak basis where the charged current and the charged lepton masses are diagonal, the lepton mixing matrix is unitary matrix that relates the neutrino weak eigenstates to the neutrino mass eigenstates as

$$\nu_\alpha = U_{\alpha i}\nu_i \tag{2.87}$$

In following section, we describe neutino oscillation in the context of three flavor. The detailed expressions are given in APPENDIX A.

2.2.1 Two Flavor Neutrino Oscillation

In the case of two flavor oscillations $\nu_\alpha \rightleftharpoons \nu_{\alpha'}$ (where $\alpha' \neq \alpha$ and α, α' represents for μ,e or τ), the oscillation probability can be derived as (see APPENDIX A)

$$P(\nu_\alpha \longrightarrow \nu_{\alpha'}) = \mid \delta_{\alpha'\alpha} + U_{\alpha' 2}U^*_{\alpha 2}(e^{-i\Delta m^2_{12}\frac{L}{2p}} - 1) \mid^2 . \tag{2.88}$$

For $\alpha' \neq \alpha$

$$P(\nu_\alpha \longrightarrow \nu_{\alpha'}) = P(\nu_{\alpha'} \longrightarrow \nu_\alpha) = \frac{1}{2}A_{\alpha'\alpha}(1 - cos\Delta m^2\frac{L}{2p}). \tag{2.89}$$

Here $A_{\alpha':\alpha}$, the amplitude of oscillation is equal to

$$A_{\alpha':\alpha} = 4 \mid U_{\alpha' 2} \mid^2 \mid U_{\alpha 2} \mid^2, \tag{2.90}$$

and $\Delta m^2 = m^2_2 - m^2_1$. Since the mixing matrix is unitary

$$\mid U_{\alpha 2} \mid^2 + \mid U_{\alpha' 2} \mid^2 = 1, \tag{2.91}$$

one can introduce the mixing angle θ as

$$| U_{\alpha 2} |^2 = \sin^2\theta, \;\; | U_{\alpha' 2} |^2 = \cos^2\theta. \tag{2.92}$$

Therefore, transition amplitude $A_{\alpha':\alpha}$ becomes

$$A_{\alpha':\alpha} = \sin^2 2\theta. \tag{2.93}$$

Then the survival probabilities $P(\nu_\alpha \longrightarrow \nu_\alpha)$ and $P(\nu_{\alpha'} \longrightarrow \nu_{\alpha'})$ can be obtained from Eqn.2.88 or from the condition of $P(\nu_\alpha \longrightarrow \nu_\alpha) + P(\nu_\alpha \longrightarrow \nu_{\alpha'}) = 1$. Therefore, one gets

$$P(\nu_\alpha \longrightarrow \nu_\alpha) = P(\nu_{\alpha'} \longrightarrow \nu_{\alpha'}) = 1 - \frac{1}{2}\sin^2 2\theta(1 - \cos\frac{\Delta m^2 L}{2p}). \tag{2.94}$$

Thus in the case of two neutrinos, the transition probabilities are determined by parameters $\sin^2 2\theta$ and Δm^2.

Besides survival probability, the transition, or oscillation probability for $P(\nu_\alpha \longrightarrow \nu_{\alpha'})$ can be found as

$$P(\nu_\alpha \longrightarrow \nu_{\alpha'}) = \frac{1}{2}\sin^2 2\theta(1 - \cos 2\pi\frac{L}{L_0}). \tag{2.95}$$

Here L_0 is the oscillation length and has the value,

$$L_0 = 4\pi\frac{E}{\Delta m}. \tag{2.96}$$

If one substitutes this oscillation length into the Eqn. 2.95, oscillation probability can rewritten in terms of the neutrino mass difference Δm^2, the distance, L, and neutrino energy, E, as

$$P(\nu_\alpha \longrightarrow \nu_{\alpha'}) = \frac{1}{2}\sin^2 2\theta(1 - 2.54\cos\Delta m^2\frac{E}{L}). \tag{2.97}$$

As seen in Eqn. 2.97, the transition probability depends periodically on L/E. When $2.54\Delta m^2(L/E) = \pi(2n+1)$ is satisfied the transition probability is maximum and it is equal to $\sin^2 2\theta$. On the other hand, when $2.54\Delta m^2(L/E) = \pi n$, transition probability is zero. In order to observe neutrino oscillation the parameter Δm^2 must be large enough so that the condition $\Delta m^2(L/E) \geq 1$ is satisfied.

2.2.2 Three Flavor Neutrino Oscillation

We will now consider here the minimal scheme of three-neutrino mixing

$$\nu_\alpha = \sum_{i=1}^{3} U_{\alpha i}\nu_i, \tag{2.98}$$

where ν_α stands for the neutrino flavors, ν_i stands for mass eigenstates and U is the 3×3 PMNS mixing matrix

$$\begin{pmatrix} U_{e1} & U_{e2} & U_{e3} \\ U_{\mu 1} & U_{\mu 2} & U_{\mu 3} \\ U_{\tau 1} & U_{\tau 2} & U_{\tau 3} \end{pmatrix}$$

Substituting ν_α, ν_i and U into the Eqn.2.116, one gets

$$\begin{pmatrix} \nu_e \\ \nu_\mu \\ \nu_\tau \end{pmatrix} = \begin{pmatrix} U_{e1} & U_{e2} & U_{e3} \\ U_{\mu 1} & U_{\mu 2} & U_{\mu 3} \\ U_{\tau 1} & U_{\tau 2} & U_{\tau 3} \end{pmatrix} \begin{pmatrix} \nu_1 \\ \nu_2 \\ \nu_3 \end{pmatrix}$$

This scheme provides two independent Δm^2's. Let us start with the consideration of neutrino oscillation in the atmospheric range of Δm^2,which can be explored in the atmospheric and long baseline accelerator and reactor neutrino experiments. By using Eqn.A15 in the APPENDIX A with $m_1 < m_2 < m_3$ there are two possibilities:

1. Hierarchy of neutrino mass-squared differences $\Delta m^2_{21} \simeq \Delta^2_{sol}$; $\Delta m^2_{32} \simeq \Delta m^2_{atm}$; $\Delta m^2_{21} \ll \Delta^2_{32}$

2. Inverted hierarchy of neutrino mass-squared differences $\Delta m^2_{32} \simeq \Delta^2_{sol}$; $\Delta m^2_{21} \simeq \Delta^2_{atm}$; $\Delta m^2_{32} \ll \Delta m^2_{21}$.

First, lets assume that the neutrino mass spectrum is the type 1. The values of L/E, relevant for neutrino oscillations in the atmospheric range of neutrino mass-squared difference, satisfy the inequality:

$$\Delta m^2_{21} \frac{L}{E} \ll 1 \tag{2.99}$$

Thus, contribution of Δm^2_{21} to the transition probability in Eqn.A15 can be neglected. In this case, for the probability of the transition $\nu_\alpha \longrightarrow \nu_{\alpha'}$ the following expression is obtained,

$$P(\nu_\alpha \longrightarrow \nu_{\alpha'}) \simeq \mid \delta_{\alpha'\alpha} + U_{\alpha' 3} U^*_{\alpha 3} (e^{-i\Delta m^2_{32} \frac{L}{2E}} - 1) \mid^2 . \tag{2.100}$$

Hence, in the leading approximation,the transition probabilities in the atmospheric range of Δm^2 are determined by the largest neutrino mass- squared difference Δm^2_{32} and by the elements of the third column of the neutrino mixing matrix, which connect the flavor neutrino field $\nu_{\alpha L}$ with the field of the heaviest neutrino ν_{3L}. For the appearance probability we obtain from

Eqn.A15 the expression

$$P(\nu_\alpha \longrightarrow \nu_{\alpha'}) = \frac{1}{2} A_{\alpha';\alpha}(1 - \cos \Delta m^2_{32} \frac{L}{2E})(\alpha \neq \alpha') \tag{2.101}$$

where the oscillation amplitude is given by

$$A_{\alpha'\alpha} = 4 \mid U_{\alpha' 3} \mid^2 \mid U_{\alpha 3} \mid^2 . \tag{2.102}$$

The survival probability can simply obtained as

$$P(\nu_\alpha \longrightarrow \nu_\alpha) = 1 - \sum_{\alpha' \neq \alpha} P(\nu_\alpha \longrightarrow \nu_{\alpha'}) = 1 - \frac{1}{2} B_{\alpha;\alpha}(1 - \cos \Delta m^2_{32} \frac{L}{2E}). \tag{2.103}$$

Taking into account the unitarity of the mixing matrix, the amplitude $B_{\alpha;\alpha}$ can be written as:

$$B_{\alpha;\alpha} = \sum_{\alpha' \neq \alpha} A_{\alpha';\alpha} = 4 \mid U_{\alpha 3} \mid^2 (1 - \mid U_{\alpha 3} \mid^2). \tag{2.104}$$

For the case of inverted hierarchy of the neutrino mass, the transition probabilities can be obtained from Eqn. 2.101 – 2.104 by replacing Δm^2_{32} with Δm^2_{21} and $\mid U_{\alpha 3} \mid^2$ with $\mid U_{\alpha 1} \mid^2$. We notice that transition probability depends only on $\mid U_{\alpha 3} \mid^2$ and Δm^2_{32}. The transition probabilities Eqn.2.101 and Eqn.2.103 have a two-neutrino form in each channel. This is the obvious consequence of the fact that only the largest mass-squared difference Δm^2_{32} contributes to the transition probabilities. The elements $\mid U_{\alpha 3} \mid^2$, which determine the oscillation amplitudes, satisfy the unitarity condition $\sum_\alpha \mid U_{\alpha 3} \mid^2 = 1$. Hence transition probabilities are characterized by three parameters. Δm^2_{32}, $\sin^2 \theta_{23}$, $\mid U_{\alpha 3} \mid^2$.

2.2.2.1 Neutrino Oscillation in Solar Range

Let us consider now, solar neutrino oscillations. Since the solar neutrinos are ν_e, one can write the survival probability for ν_e which is produced in the Sun and reached to the earth as,

$$P(\nu_e \longrightarrow \nu_e) = \mid \sum_{i=1,2} \mid U_{ei} \mid^2 e^{-i\Delta m^2_{i1} \frac{L}{2E}} + \mid U_{e3} \mid^2 e^{-i\Delta m^2_{31} \frac{L}{2E}} \mid^2 . \tag{2.105}$$

We are interested in the ν_e survival probability averaged over the region where neutrinos are produced. Because of the hierarchy $\Delta m^2_{32} \gg \Delta m^2_{21}$, the interference between first and second term in Eqn.2.105 disappears. The averaged survival probability can be presented in the form

$$P(\nu_e \longrightarrow \nu_e) = \mid U_{e3} \mid^4 + (1 - \mid U_{e3} \mid^2)^2 P^{(1,2)}(\nu_e \longrightarrow \nu_e) \tag{2.106}$$

where $P^{(1,2)}(\nu_e \longrightarrow \nu_e)$ is given by

$$P^{(1,2)}(\nu_e \longrightarrow \nu_e) = 1 - \frac{1}{2}A^{(1,2)}(1 - \cos \Delta m^2_{21}\frac{L}{2E}), \tag{2.107}$$

where

$$A^{(1,2)} = 4\frac{\mid U_{e1} \mid^2 \mid U_{e2} \mid^2}{(1- \mid U_{e3} \mid^2)^2}. \tag{2.108}$$

Hence the ν_e survival probability is characterized, in the solar range of Δm^2, by three parameters Δm^2_{21}, $tan^2_{\theta_{12}}$, $\mid U_{e3} \mid^2$. The only common parameter for the atmospheric and solar ranges of Δm^2 is $\mid U_{e3} \mid^2$.

2.2.2.2 $\nu_\mu \rightarrow \nu_\tau$ Oscillation

In the three flavor neutrino oscillation section the relation

$$\begin{pmatrix} \nu_e \\ \nu_\mu \\ \nu_\tau \end{pmatrix} = \begin{pmatrix} U_{e1} & U_{e2} & U_{e3} \\ U_{\mu 1} & U_{\mu 2} & U_{\mu 3} \\ U_{\tau 1} & U_{\tau 2} & U_{\tau 3} \end{pmatrix} \begin{pmatrix} \nu_1 \\ \nu_2 \\ \nu_3 \end{pmatrix}$$

has been written and it is stated that by assuming $m_1 < m_2 < m_3$, there are two mass hierarchy.

1. Hierarchy of neutrino mass-squared differences $\Delta m^2_{21} \simeq \Delta^2_{sol}; \Delta m^2_{32} \simeq \Delta m^2_{atm}; \Delta m^2_{21} \ll \Delta^2_{32}$
2. Inverted hierarchy of neutrino mass-squared differences $\Delta^2_{32} \simeq \Delta^2_{sol}; \Delta m^2_{21} \simeq \Delta^2_{atm}; \Delta m^2_{32} \ll \Delta m^2_{21}$.

In the case of $\nu_\mu \rightarrow \nu_\tau$ oscillation, first mass hierarchy that is atmospheric mass hierarchy is used. From the general formalism of neutrino oscillation that is derived in Appendix A one has

$$|\langle \nu_{\alpha'} | \nu_\alpha \rangle|^2 = |\delta_{\alpha\alpha'} + \sum U^*_{\alpha i} U_{\alpha' i}(e^{-i\Delta m^2_{12}\frac{L}{2p}} - 1)|^2. \tag{2.109}$$

Or in other words

$$P(\nu_\alpha \rightarrow \nu_{\alpha'}) = |\delta_{\alpha\alpha'} + \sum U^*_{\alpha i} U_{\alpha' i}(e^{-i\Delta m^2_{12}\frac{L}{2p}} - 1)|^2, \tag{2.110}$$

where the Δm^2_{12} term stands for the mass square difference of ν_α and $\nu_{\alpha'}$. For the atmospheric mass hierarchy the only dominant mass term will be Δm^2_{32}. Since

$$\Delta m^2_{21}\frac{L}{E} \ll 1, \tag{2.111}$$

the contribution of Δm^2_{21} can be neglected. Then one obtains

$$P(\nu_\mu \to \nu_\tau) = |\delta_{\mu\tau} + U^*_{\alpha 3} U_{\alpha' 3}(e^{-i\Delta m^2_{32}\frac{L}{2p}} - 1)|^2, \tag{2.112}$$

where $\delta_{\mu\tau} = 0$. So

$$= |U^*_{\alpha 3} U_{\alpha' 3}(e^{-i\Delta m^2_{32}\frac{L}{2p}} - 1)|^2, \tag{2.113}$$

$$= |U^*_{\alpha 3} U_{\alpha' 3} e^{-i\Delta m^2_{32}\frac{L}{2p}} - U^*_{\alpha 3} U_{\alpha' 3}|^2 \tag{2.114}$$

$$= |U^*_{\alpha 3} U_{\alpha' 3}(\cos \Delta m^2_{32}\frac{L}{2p} - i \sin \Delta m^2_{32}\frac{L}{2p}) - U^*_{\alpha 3} U_{\alpha' 3}|^2. \tag{2.115}$$

$$\tag{2.116}$$

Considering only the real parts, one gets

$$= |(U^*_{\alpha 3} U_{\alpha' 3})(\cos \Delta m^2_{32}\frac{L}{2p} - 1)|^2 \tag{2.117}$$

$$= |U^*_{\alpha 3}|^2 |U_{\alpha' 3}|^2(\cos \Delta m^2_{32}\frac{L}{2p} - 1)|^2 \tag{2.118}$$

$$= |U^*_{\alpha 3}|^2 |U_{\alpha' 3}|^2(\cos^2 \Delta m^2_{32}\frac{L}{2p} - 2\cos \Delta m^2_{32}\frac{L}{2p} + 1)|. \tag{2.119}$$

$$\tag{2.120}$$

We assume that $\cos^2 \Delta m^2_{32}\frac{L}{2p} \simeq 1$ then

$$= |U^*_{\alpha 3}|^2 |U_{\alpha' 3}|^2(2 - 2\cos \Delta m^2_{32}\frac{L}{2p}) \tag{2.121}$$

$$= 2|U^*_{\alpha 3}|^2 |U_{\alpha' 3}|^2(1 - \cos \Delta m^2_{32}\frac{L}{2p}). \tag{2.122}$$

$$\tag{2.123}$$

Defining the oscillation parameter $A_{\alpha'\alpha} = 4|U^*_{\alpha 3}|^2 |U_{\alpha' 3}|^2$, the oscillation probability becomes

$$P(\nu_\mu \to \nu_\tau) = \frac{1}{2} A_{\alpha'\alpha}(1 - \cos \Delta m^2_{32}\frac{L}{2p}). \tag{2.124}$$

Lets introduce $|U^*_{\alpha 3}|^2 = \cos^2 \theta_{23}$ and $|U_{\alpha' 3}|^2 = \sin^2 \theta_{23}$ where θ_{23} is the mixing angle, the oscillation amplitude becomes $A_{\alpha'\alpha} = \sin^2 2\theta$. Then, oscillation probability of $\nu_\mu \to \nu_\tau$ becomes,

$$P(\nu_\mu \to \nu_\tau) = \frac{1}{2} \sin^2 2\theta(1 - \cos \Delta m^2_{32}\frac{L}{2p}). \tag{2.125}$$

Defining the oscillating length as $L_0 = 4\pi\frac{E}{\Delta m^2}$ one gets

$$P(\nu_\mu \to \nu_\tau) = \frac{1}{2} \sin^2 2\theta(1 - \cos 2\pi\frac{L}{L_0}), \tag{2.126}$$

or,

$$P(\nu_\mu \to \nu_\tau) = \frac{1}{2} \sin^2 2\theta(1 - \cos 2.53\Delta m^2 \frac{L}{E}). \tag{2.127}$$

CHAPTER 3

THE OPERA EXPERIMENT

OPERA (**O***scillation* **P***ro ject with* **E***mulsion t***R***acking* **A***pparatus*)[9] is a long baseline experiment which was designed to search the direct observation of ν_τ appearance from $\nu_\mu \rightarrow \nu_\tau$ oscillations in the CNGS beam. The OPERA detector is located in LNGS Underground laboratory in Italy, 730 km away from CERN. The OPERA detector is a hybrid set-up which combines lead/emulsion target(ECC) with various electronic detectors. The main part of the experiment is the Emulsion Cloud Chamber(ECC) which is standalone detector to measure electromagnetic showers and charged particle momentum as well as it acts as a target for neutrino interactions.

The construction of the detector was started in 2003 and finished in the summer of 2008. The physics run with full detector took place in 2008. The data taking phase of the experiment is expected to last at least five years.

3.1 The OPERA-CNGS Beam

The OPERA experiment uses the CNGS (**C**ERN **N**eutrinos to **G**ran **S**asso) beam produced in CERN[27]. The beam is optimized to study of $\nu_\mu \rightarrow \nu_\tau$ oscillation in appearance mode.

The CNGS Beam is produced by using the 400 GeV protons that are accelerated in CERN-SPS. Then, these protons hit 2m long graphite target producing pions and kaons which are focused into a parallel beam using magnetic lenses; horn and reflector as shown in Figure 3.1. After that, there is 1 km long decay channel for pions and kaons. In this decay channel most of the pions and kaons decay to muon, muon neutrinos and to soft hadrons. At the end of the decay tube, there is a hadron stopper that stops hadrons and some of the muons. The

remaining charged particles are absorbed by the rock while neutrinos continue their travel towards LNGS. As a result, nearly a pure muon neutrino beam at average energy of 17 GeV has been produced. The beam features are given in Table 3.1.

Table 3.1: Properties of nominal ν_μ-CNGS neutrino beam.

$\nu_\mu(m^{-2}/pot)$	7.45×10^{-9}
$\nu_\mu CC/pot/kton$	5.44×10^{-17}
$< E >_\nu (GeV)$	17
$(\nu_e + \bar{\nu_e})/\nu_\mu$	0.85%
$\bar{\nu_\mu}/\nu_\mu$	2.0%
ν_τ *prompt*	Negligible

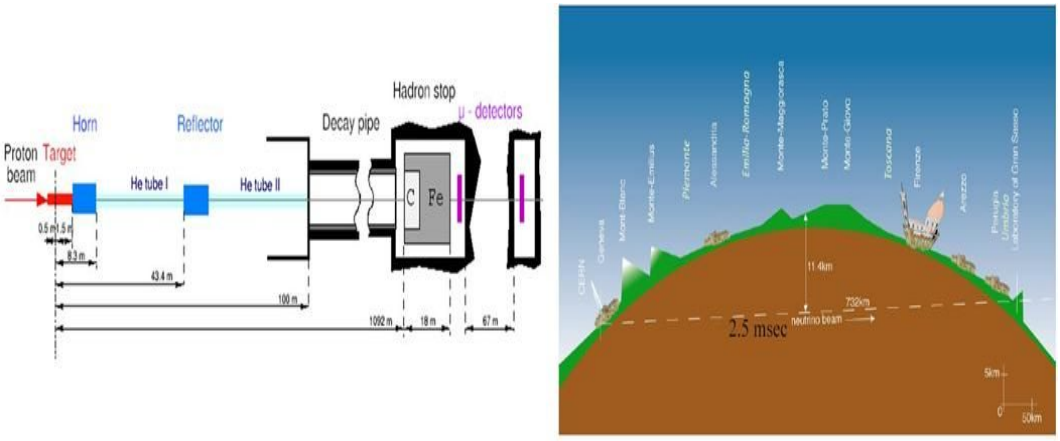

Figure 3.1: CNGS beam lay-out and representation.

The expected rate of ν_μ CC interaction is about 2600/kton/year. The number of ν_τ CC events for $sin^2 2\theta$=1 and two values of Δm^2 is given in Table 3.2.

3.2 The OPERA Detector

The OPERA apparatus consists of two identical parts, called Super-Modules(SM). Each SM has target section and muon spectrometer. The target section is constituted by 31 walls and target tracker planes(TT). Each wall plane is followed by a TT that provide real-time tracking of charged particles. The bricks are placed in walls that house 3328 brick per plane. Therefore, the total number of bricks hosted in the two target section is about 150,000 which corresponds

Table 3.2: Expected number of events in 5 years run with nominal beam intensity for different values of mass difference Δm^2_{23}.

Decay Channel	Signal $\Delta m^2_{23} = 2.5 \times 10^{-3} eV^2$	Signal $\Delta m^2_{23} = 3.0 \times 10^{-3} eV^2$
$\tau \rightarrow \mu$	2.9	4.2
$\tau \rightarrow e$	3.5	5.0
$\tau \rightarrow h$	3.1	4.49
$\tau \rightarrow 3h$	0.	1.3
total	10.4	14.9

to a mass of 1.25 kton. In order to produce this amount of brick, a dedicated machine which is called Brick Assembling Machine(BAM) was designed. The produced bricks in BAM are then placed in the brick walls by means of automatic system called Brick Manipulator System(BMS). BMS is able to extract the bricks tagged by electronic detectors.

Muon identification and charge measurement are performed by the muon spectrometer which consists of a dipolar magnet. The electronic detectors reconstruct tracks and predict the brick where neutrino interaction is occurred. In Figure 3.2 picture of the OPERA detector can be seen. In the following we describe some technical properties and principle aims of all sub-detectors of the OPERA detector.

3.2.1 The OPERA Brick

A ECC brick is made of 56 lead plates(1mm thick) interleaved with nuclear emulsions for a total weight of 8.3 kg. The lead plate is used as target and emulsion film is used as tracking device. Nuclear emulsions are still remains to be only detector providing three dimensional position information with a sub-micron resolution. Hence emulsion is particularly suited for observing short-lived particles like τ^- lepton. The OPERA films consists of 2 emulsion layers(44 μm each) on both sides of the 205μm thick plastic base as can be seen in Figure 3.3. Emulsion doublets called as Changeable Sheet(CS) are attached to the downstream of each brick as can be seen in Figure 3.4. CS is used as an interface between electronic detector and ECC. Hence, guiding the vertex-finding procedure.

The use of passive material allows for momentum measurement of charged particles, identification and measurement of electromagnetic showers and electron/pion separation. The use of

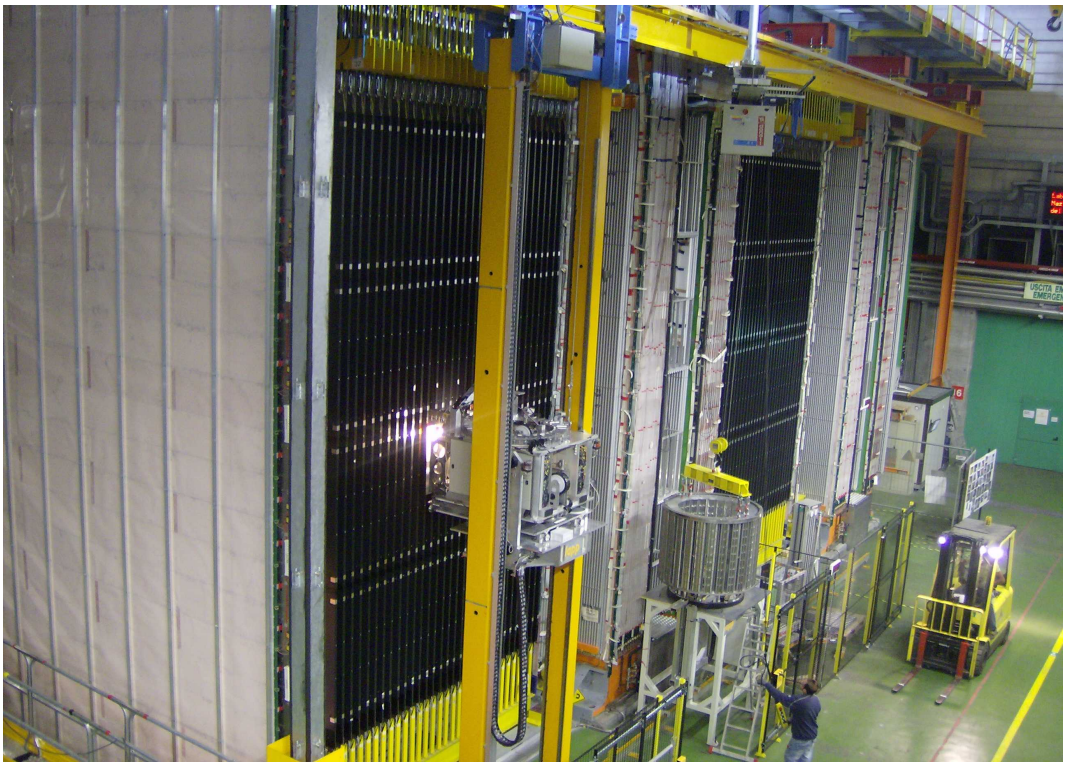

Figure 3.2: The OPERA detector in INFN-LNGS Hole-C.

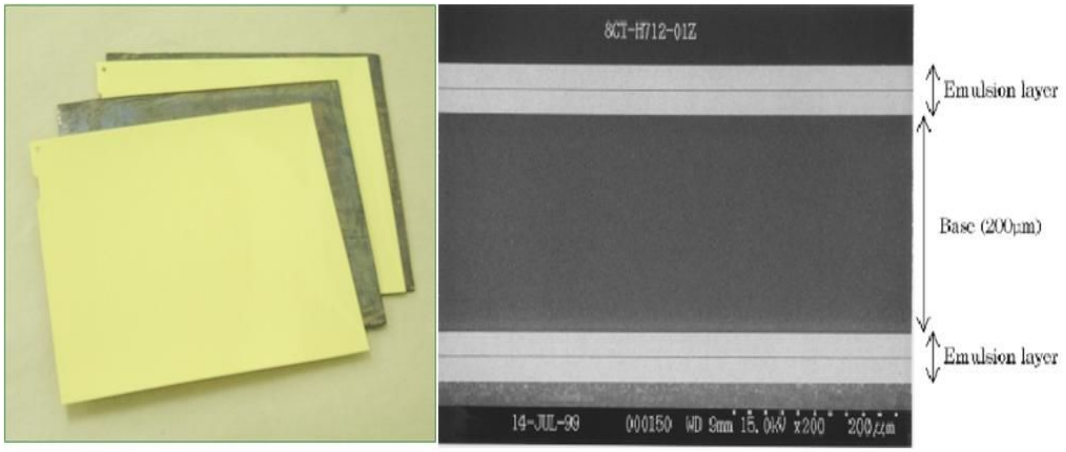

Figure 3.3: The OPERA experiment emulsions and microscopic view of the emulsion.

ECC technology in high energy experiments goes back to 1945's. It was used in experiments that have studied cosmic-rays soon after the second world war and leading the discovery of the charm particles in 1971. More recently it was successfully used in the DONUT experiment to observe ν_τ interactions.

Figure 3.4: The OPERA experiment emulsion claud chamber (ECC) and Changeable Sheet (CS) that is attached to ECC.

3.2.2 The OPERA Target Tracker

Each brick wall is interleaved with two electronic TT. The main task of the target tracker detector is to locate the brick where neutrino interaction has occurred. The target trackers have 2 planes, each is made of 4 horizontal and 4 vertical modules that have scintillation with 6.6m long, 2.6 cm wide and 1 cm thick. For read out, multi anode, and 64 pixel photomultipliers are placed at both ends of the fibers as shown in Figure 3.5

3.2.3 The OPERA Spectrometers

In the OPERA apparatus, both SMs end with the muon spectrometer. The main task of the muon spectrometer is to measure the muon momentum and it's charge. The expected performance of the spectrometer is to reduce the charge confusion less then 0.3% and gives a

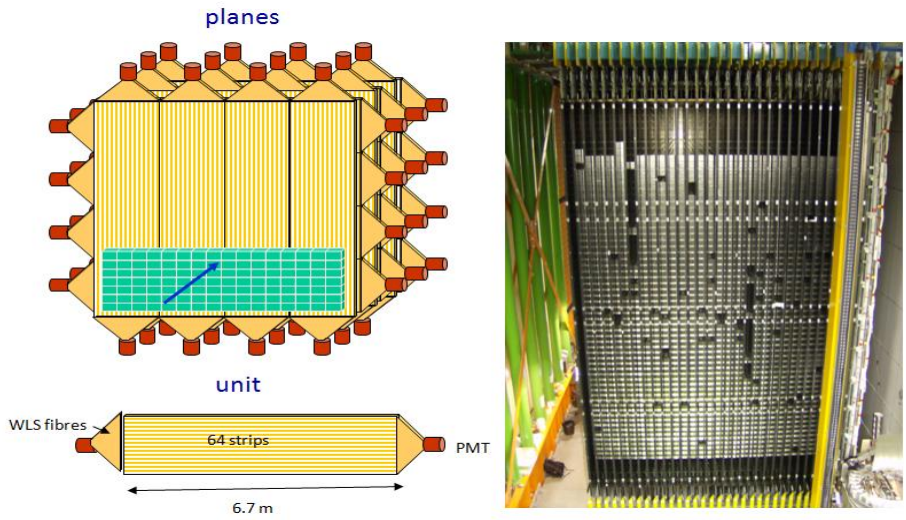

Figure 3.5: Schematic view and picture of the OPERA Target Trackers (TT).

momentum resolution better than 20% for momentum less then 50 GeV. The muon identification efficiency reaches 95% by adding the target tracker information. The information from the spectrometer is used for the classification of neutrino events. The OPERA muon spectrometers are consist of electronic RPC(Inner Tracker), Drift Tubes(Precision Trackers) and Dipolar Magnet as shown in Figure 3.6.

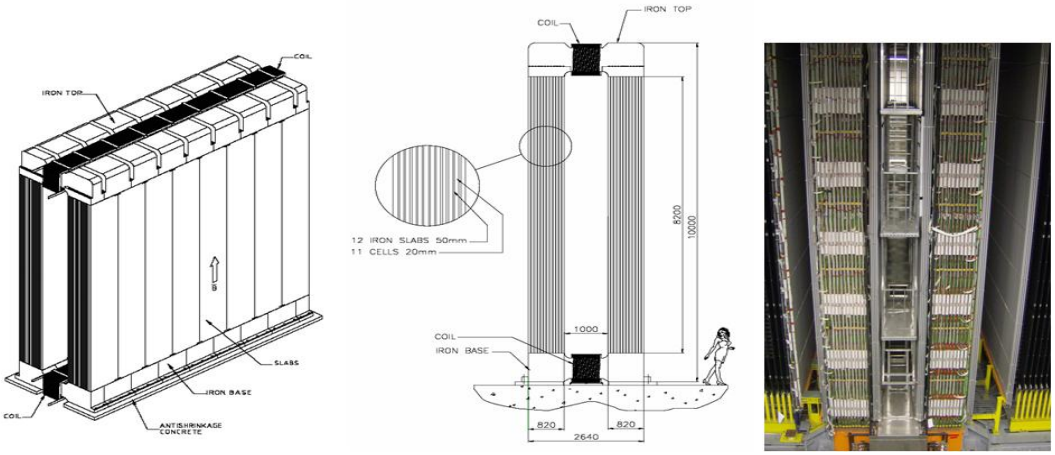

Figure 3.6: Schematic view and picture of the OPERA spectrometer.

Dipolar magnet has two parts, interleaved by drift tubes and consists of 12 iron walls. These iron-walls are magnetized by using AC source of I=1600A, which produces 1.55T magnetic field, transverse to the neutrino beam axis. Each spectrometer is equipped with six vertical

planes of drift tubes as precision tracker together with 22 planes of RPC bakelite chambers reaching a spatial resolution of $1cm$ and an efficiency of 96%.

The iron walls are surrounded by the RPC's. RPC's are made of $1.1x2.9m^2$ high resistivity bakelite slabs.

3.3 The OPERA Physics Performance

3.3.1 τ Detection

The signature of $\nu_\mu \rightarrow \nu_\tau$ oscillation is the of τ CC interaction and subsequent decay vertex of τ^- lepton. Considering τ^- lepton, decay channels are[28].

$$\tau^- \rightarrow e^- \nu_\tau \overline{\nu_e}, \quad BR = 17.8\%$$

$$\tau^- \rightarrow \mu^- \nu_\tau \overline{\nu_\mu}, \quad BR = 17.7\%$$

$$\tau^- \rightarrow h^- \nu_\tau (n\pi^0), \quad BR = 49.5\%.$$

So, observing these decay channels will lead us to observe $\nu_\mu \rightarrow \nu_\tau$ oscillation. The flight length distribution of τ lepton is shown in Figure 3.7. The mean τ decay length is $450\mu m$.

The ECC detector is very convenient to identify electron by measuring its shower. Therefore, electron channel can be studied at high efficiency. Concerning muon channel, we require that energy of muon lies in the range 1-15 GeV. The lower cut allows to reject background from the low energy hadrons. The upper cut reduces ν_τ CC events about 30% with a small loss of signal. The hadronic channel has the biggest branching ratio. In order to reduce background to this channel as low as possible, strong kinematical cuts are applied both at the decay and at the primary vertex.

The decay topologies of τ lepton are classified as short and long decays as seen in Figure 3.8. Long decays correspond to the case where tau decay occurs in the first or second downstream plates. In the case of short decays, τ decay vertex and neutrino interaction vertex are in the same lead plate. The short τ decays are selected on the basis of the impact parameter of the τ daughter track with respect to the primary vertex. The long τ decay can be identified by measuring kink angle between the τ and the daughter track. These channels have been

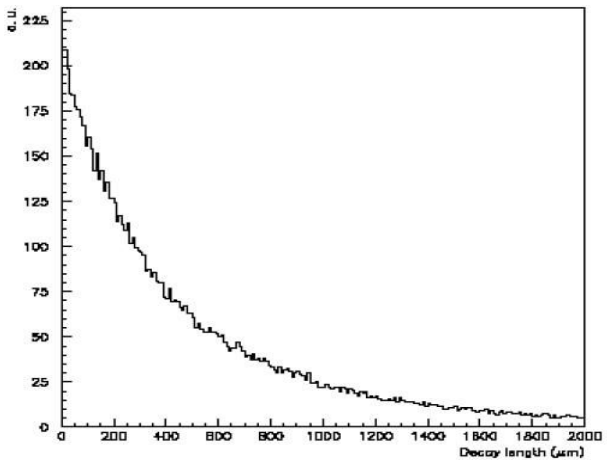

Figure 3.7: τ decay length distribution.

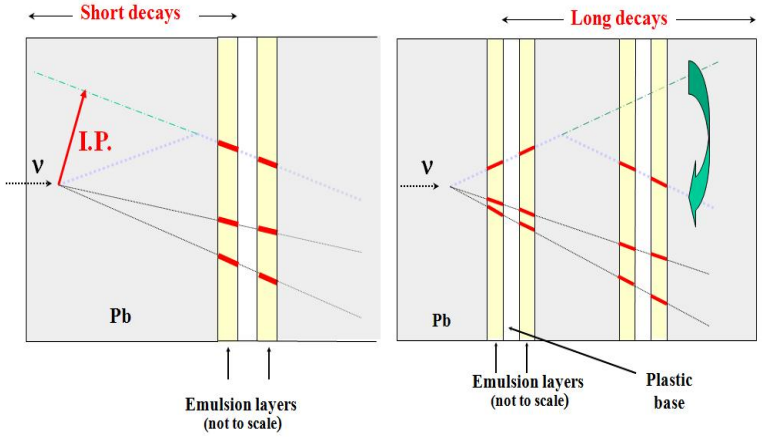

Figure 3.8: Schematic view of long and short decay of τ in Emulsion Cloud Chamber.

studied in the experiment and the overall detection efficiencies, including the BR, can be found in Table 3.2.

Table 3.3: τ detection efficiencies (including branching ratios) for the OPERA experiment. Overall efficiencies are weighted sum on DIS and QE events.

	DIS Long	QE Long	DIS Short	Overall
$\tau \to e$	2.7 %	2.3 %	1.3 %	3.4 %
$\tau \to \mu$	2.4 %	2.5 %	0.7 %	2.8 %
$\tau \to h$	2.8 %	3.5 %	–	2.9 %
total	8.0 %	8.3 %	2.1 %	9.1 %

3.3.2 The Background Source To Oscillation Signal

The main background to oscillation signal in the OPERA experiment can be described as follows:

- The large angle scattering of muon in ν_μCC interaction. This background can be suppressed by applying cuts to the kink angle and transverse muon momentum in the decay vertex (kink angle $\theta > 20$ mrad and $p_t >$250 MeV).

- As it has been described previously, the hadron decay channel, due to the hadron re-interactions constitutes background for the τ decay if the primary muon is not identified in ν_μ CC interaction.

- Charm mesons are produced in the interaction of ν_μ with nucleon due to the reactions, $\nu_\mu N \to c\mu X$, $\nu_\mu N \to c\bar{c}\mu X$, $\nu_\mu N \to c\bar{c}\nu_\mu X$. Since the flights length and masses of the charmed mesons are similar to the τ lepton, they constitute background to $\nu_\mu \to \nu_\tau$ oscillation. The charm background will be discussed in Chapter 6 in more details.

By considering the 5 years run of the OPERA experiment, the estimated background can be found in the Table 3.4. But, background due to the neutral charm decays was not taken into account. In this thesis we give the first estimation of D^0 background to $\nu_\mu \to \nu_\tau$ oscillation.

Table 3.4: Expected number of background events (5 years run, nominal intensity) in each τ decay channel and the overall yield.

	$\tau \to e$	$\tau \to \mu$	$\tau \to h$	total
Charm background	0.210	0.010	0.162	0.382
Large angle μ scattering	–	0.116	–	0.116
Hadronic background	–	0.093	0.116	0.209
Total per channel	0.210	0.219	0.278	0.707

3.3.3 Analysis Strategy

The analysis flow chart is shown in Figure 3.9. When neutrinos coming from CERN cross the OPERA target, TT triggers the interactions and identifies the brick where interaction was occurred. Then brick is removed from the target wall by BMS. The X-ray marks as reference coordinate are printed on CS. The CS box is detached from the brick and developed in the underground facility. The emulsion scanning is performed to search for predicted tracks in the CS. If any candidate track is not found in CS, the brick is inserted back to the detector by attaching a new CS on the downstream surface. If the predicted track(s) is confirmed in CS, a lateral x-ray mark is printed on the brick. Then brick is brought to surface and exposed 12 hours to the cosmic rays. The density of 100 tracks/cm^2 is necessary for a precise plate to plate alignment. Then the brick is disassembled and developed in the developing facility. Finally emulsion films are delivered to the scanning laboratories in Europe and Japan. The found tracks in CS are followed in the brick plate by plate. If the track is missed in three consecutive plates, the first of them is defined as vertex plate. Then vertex is confirmed by scanning a volume with a transverse size of $1cm^2$ for 11 films around the stopping point.

3.4 The Data Taking

The first OPERA run took place in August 2006. A low intensity beam provided a total luminosity of 7.6×10^{17}pot. At that time there were no bricks in target section of the detector. In this first run, the synchronization of the GPS clocks between CERN and Gran Sasso was tuned. The full reconstruction of the electronic detectors date were tested. In total 319 neutrino-induced events were collected in agreement with the expectation of 300 events.

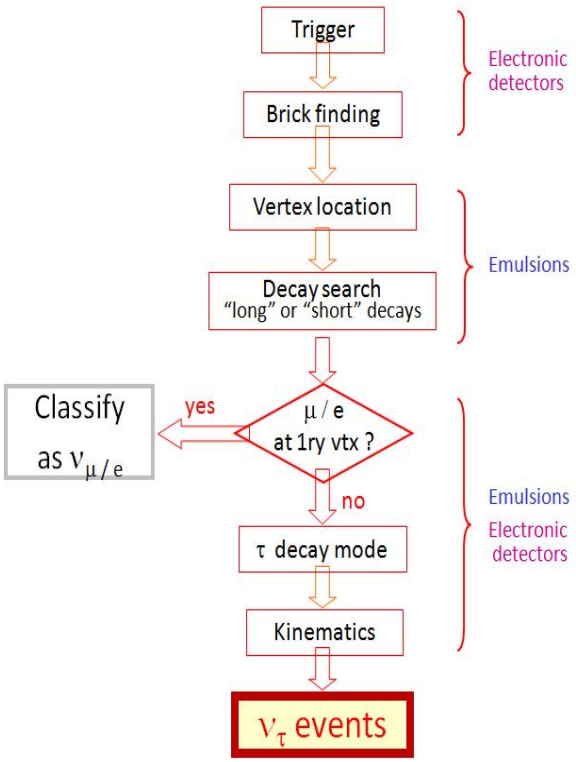

Figure 3.9: Schematic view of analysis steps in the OPERA experiment.

The first physics run took place in October 2007 with a total 8.24×10^{17} pot delivered to proton target. 38 neutrino interaction were recorded in the brick. 29 of them were reconstructed as CC and 9 of them were reconstructed as NC. This was a short run due to the problem in the ventilation control unit of the proton target of CNGS beam.

The second physics run was conducted in 2008 when 1.78×10^{19} pot were delivered to the LNGS target. The OPERA collected about 10100 events and 1700 interactions in the brick. One of those events can be seen in Figure 3.10. At the time of writing thesis, the vertex location in Europe was attempt for a sample of 73 NC and 334 CC events. Among them 58 NC and 295 CC neutrino interaction vertex have been located so far in the bricks. In the sub-sample of the located neutrino interactions, decay topologies were searched for. Two events with charm-like topologies were found.

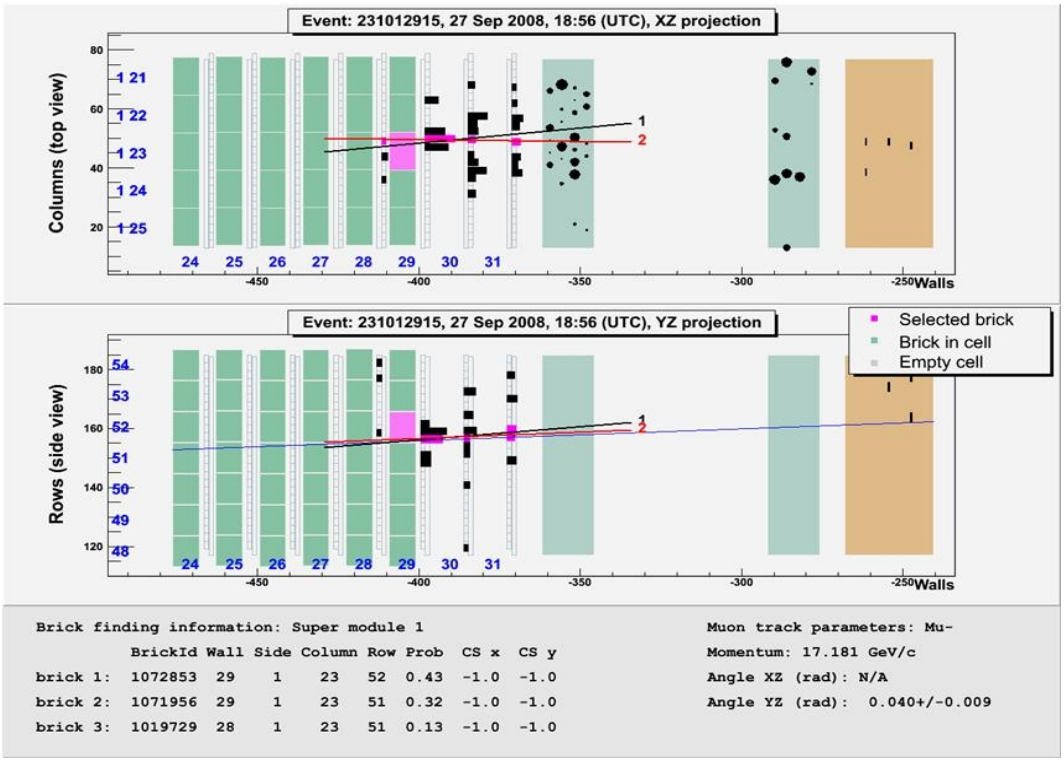

Figure 3.10: Electronic detector display of event from 2008 physical run.

3.4.1 The CS Scanning Results

The CS scanning has been performed in the scanning laboratories located in Gran Sasso and in Nagoya. As a METU group, we have contributed the CS scanning in Gran Sasso. We present the analysis of a sub-sample of scanned CS films. 559 events were scanned to search for the connection between TT and CS. The breakdown of the sample is given below,

- 9 events could not be scanned due to the high fog density in CS. The measured fog density was >30 grains/1000μm^3.
- 314 CC event were scanned and connection was found for 295 CC events
- 63 NC events were scanned and connection was found for 58 NC events.

The position and angle distributions of muon tracks in CS were shown in Figure 3.11 and in Figure 3.12. For the other tracks, distributions for position and angle can be seen in Figure 3.13 and in Figure 3.14 respectively.

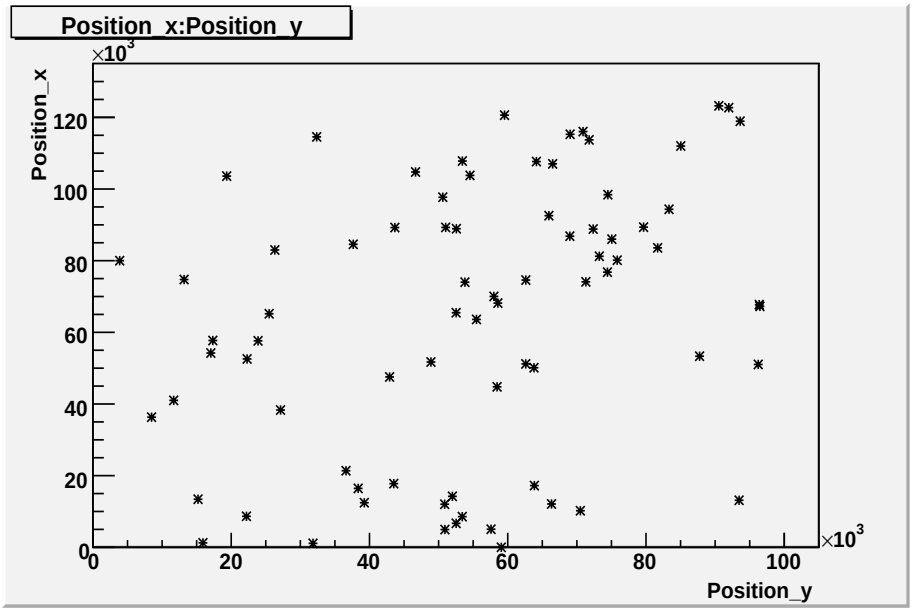

Figure 3.11: Position distribution of the found muon tracks in the CS.

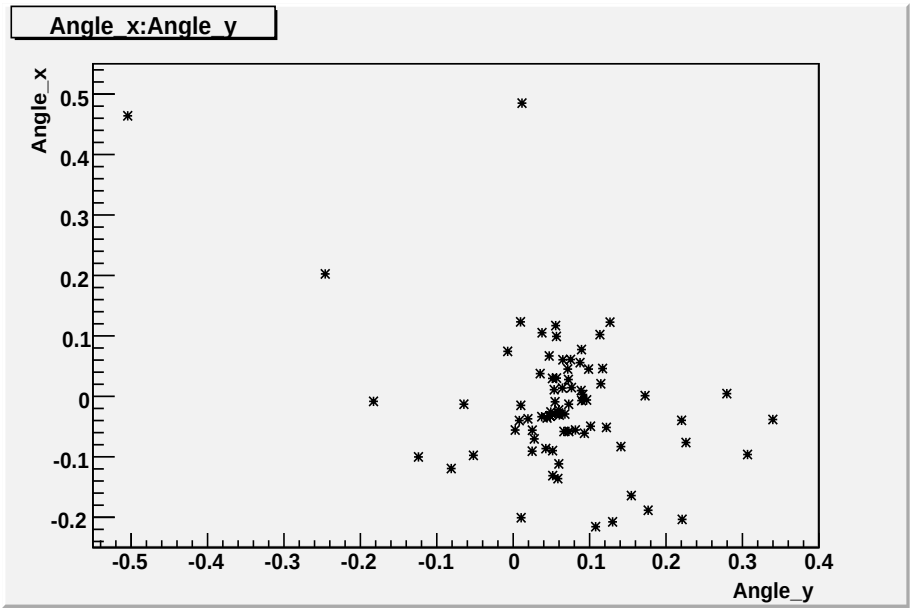

Figure 3.12: Angle distribution of the found muon tracks in the CS.

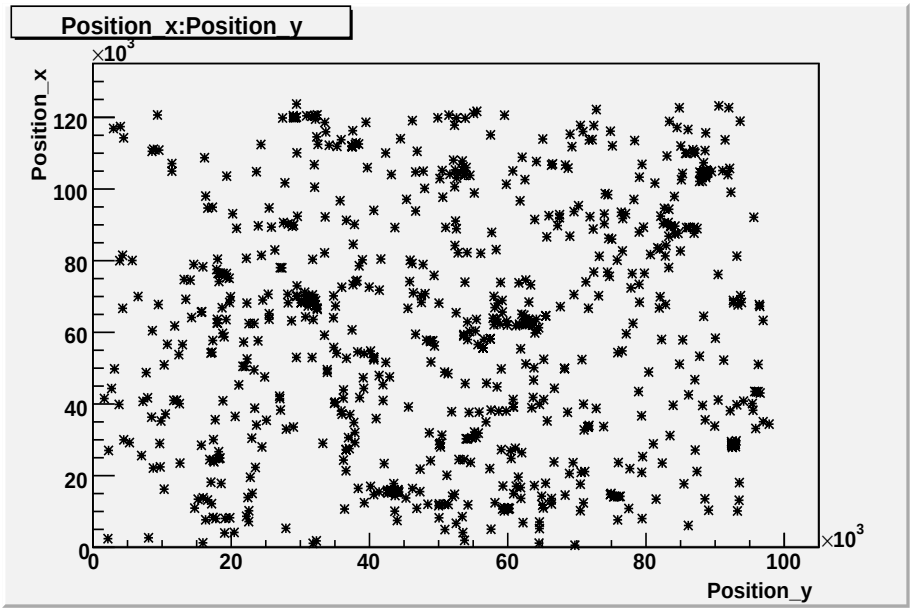

Figure 3.13: Position distribution of the found tracks other then muon in the CS.

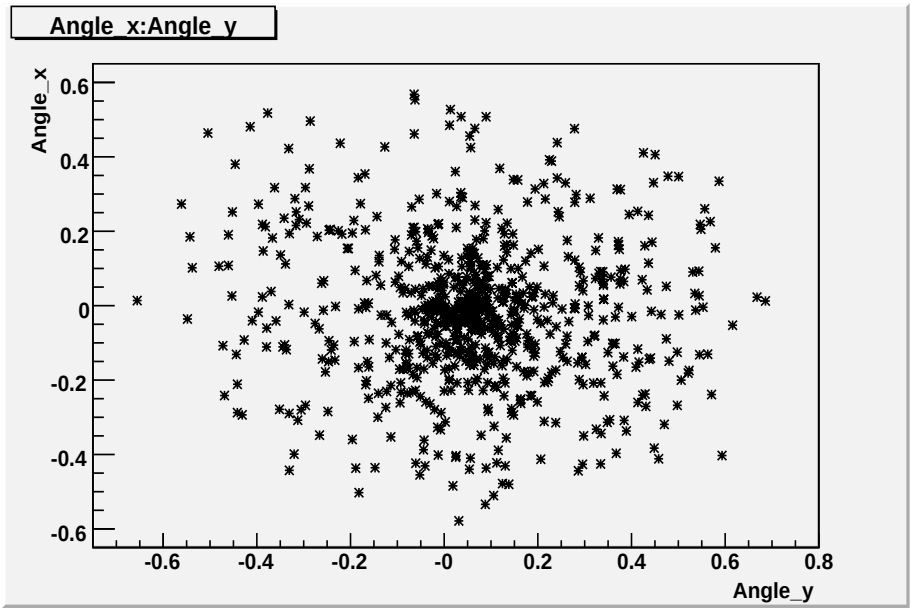

Figure 3.14: Angle distribution of the found tracks other then muon in the CS.

Finally, for the scanning efficiency of the CS, relation between the predicted and measured tracks is important. In Figure 3.15 efficiency of tracking in the CS can be seen [29].

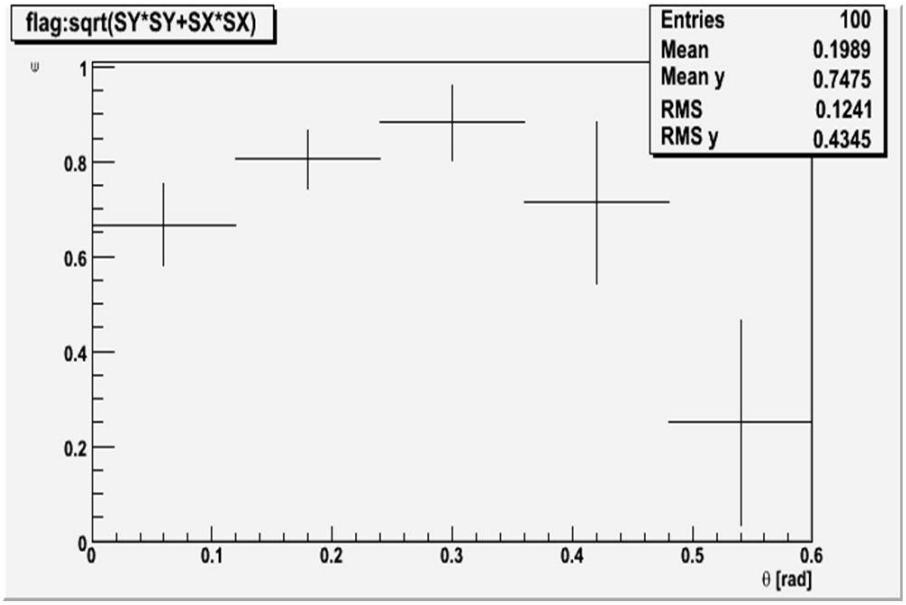

Figure 3.15: Tracking efficiency of CS scanning.

The angle and position differences between predicted and measured ones are shown in Figure 3.16 and in 3.17.

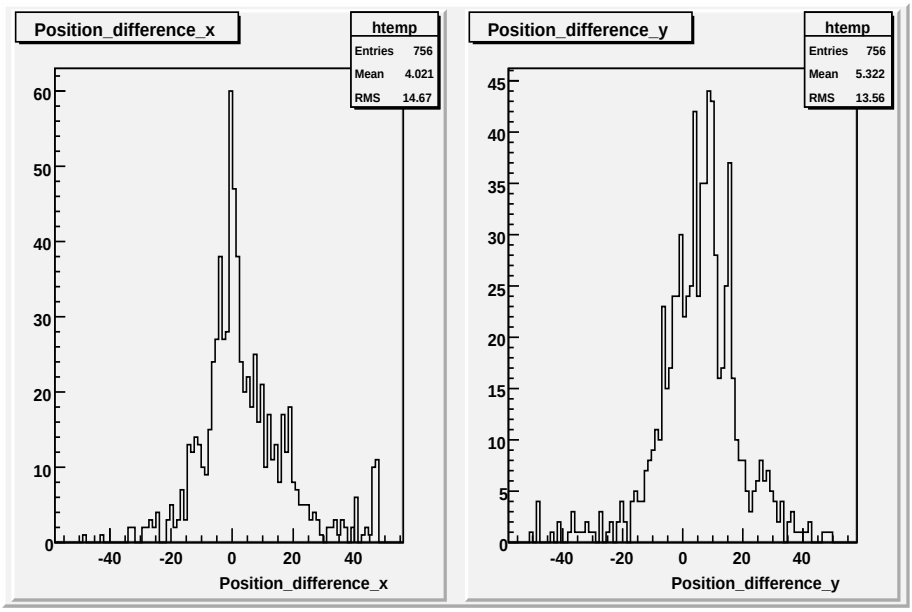

Figure 3.16: Position difference of the found tracks between two emulsion layers.

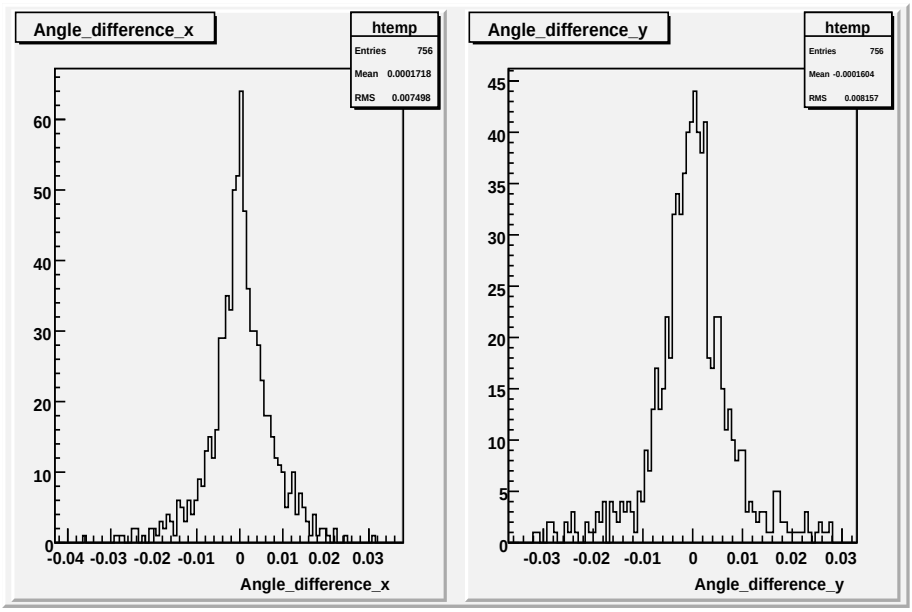

Figure 3.17: Angle difference of the found tracks between two emulsion layers.

CHAPTER 4

NUCLEAR EMULSION

In 1896, H. Becquerel observed that the photo-plates became black with the contact of salt of uranium. This is accepted as the first use of photographic emulsions in the particle physics. But, real impact was the production of first concentrated emulsions in 1946 by a chemist C. Waller. The property of those emulsions was, they had higher halide/geletin ratio which made them sensitive enough to observe the mesons tracks. As a result of new emulsions, pion was discovered in 1947 in the reaction $\pi \rightarrow \mu \rightarrow e$ [30]. In the following years, because of it's very good resolution and sensitivity emulsions have been used especially for short-lived particles search, see Table 4.1.

Table 4.1: Particles in high energy physics that were discovered by using the emulsions.

Particle	Detection Type
π^+	Emulsion
π^-	Emulsion
π^0	Counter and Emulsion
K^+	Emulsion
K^+	Emulsion
K^-	Emulsion
Σ	Emulsion
Λ	Emulsion
ν_τ	Emulsion

In recent years, due to the development of automated scanning systems, a new era for use of emulsions in the high energy experiments has started. By the help of modern scanning systems, it become possible to use large amount of emulsions in the experiments. Today, nuclear emulsions are using successfully, especially for the charm and neutrino experiments.

As an example, WA17 at CERN [31], that searched for charmed particle in neutrino CC interaction and WA75 at CERN [32] that searched for the beauty particle production induced by 350 GeV/c π beam can be shown.

The properties of emulsions that were used 50 years ago and properties of the new emulsions are nearly same. But the way that are used has changed. Nowadays emulsions are used with combination of electronic detectors. This is called hybrid set-up. In hybrid experiments, electronic detectors predict the position of particle interactions in emulsions target which are the than is scanned to search for the interaction point. CHORUS at CERN, DONUT and E531 at Fermi Lab and OPERA at INFN-LNGS are the example of hybrid setups.

The first hybrid set-up was used in the E531 experiment [33], that searched for the lifetimes of the charmed particles that had produced by Fermi Lab neutrino beam. As a result, lifetimes of D^0, $D^{\pm}$, $F^{\pm}$, Λ_c^+ were measured [34]. The CHORUS experiment [35], studied the $\nu_\mu \rightarrow \nu_\tau$ oscillation in a pure ν_μ beam and charm particle production in neutrino-nucleon interaction. The first automatic scanning was applied for the location of the neutrino interactions. The DONUT experiment [36], studied the ν_τ and it is still unique experiment that has observed the ν_τ via charged τ lepton decay.

4.1 Properties of Nuclear Emulsions

Nuclear emulsions are the composition of micro-crystal silver halides (AgBr) with a gelatin layer. There is also variable quantity of water and a little glycerol in the composition of emulsion. Nuclear emulsions are similar to the photographic emulsions except their uniformity in size and sensitivity, their size and their gelatin/AgBr ratio. Emulsions in high energy physics are used for the 3-dimensional track recording of the charged particles. While a charged particle passes the emulsion media, it creates the images that is know as ”latent image”. As a result of chemical ”development” of emulsion, latent image became visible and 3-dimensional track of the charged particle is formed.

Latent image formation is the characteristic of AgBr. When light or a charged particle passes through the emulsion medium, it releases an electron and it turns silver ion to the silver atom. And this silver atoms create the latent images which are not visible yet. But they have the property that under chemical development procedure, silver atom collection places turn into

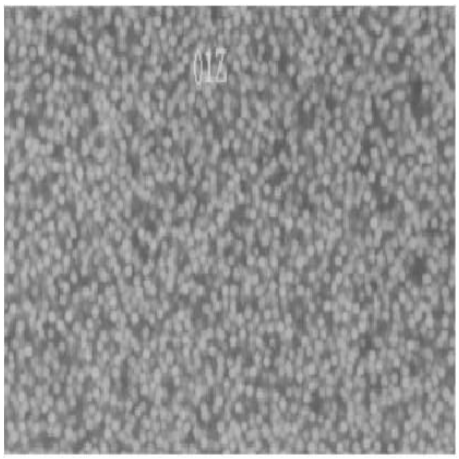

Figure 4.1: Microscopic view of nuclear emulsion crystals

metallic silver faster then the silver in the ionic net. So by choosing suitable time interval to turn just latent image to visible image the charged particle tracks can be visible.

Development is a chemical process to obtain the particle track from the latent images. It is an important feature of the AgBr emulsion that when it is placed in a reducing agent, the developer, the latent images became metallic silver and visible. The developer reduces all the latent image centers and leaved other crystal unchanged. Since development is a chemical process like all other chemical processes it depends on temperature, pH and time. If these effects do not arranged well, unwanted crystals can be developed and it can create the background known as ”fog”. After the development, in order to remove all the residual AgBr, fixation procedure should be held. The fixing agent is generally sodium or ammonium thiosulphate. Thiosulphate is solvable in the water and may be removed from emulsion by washing which brings us to the next step of development. Washing is also important for development. Emulsion should be washed thoroughly in order to remove all thiosulphate complexes. The last step of the development is to dry the emulsions in nominal temperature and humidity conditions. After all of these steps, emulsions are ready to be scanned.

There are also some effects on emulsion which are necessary to be considered. The first one is emulsion fading, which is the erasing of the latent image due to the humidity and temperature conditions. Next effect is shrinkage, which is the change in emulsion volume due to the chemical development procedure. The other effect on emulsion is distortion. Distortion is caused by the mechanical effects on emulsion and drying conditions of emulsion. Distortion

will be considered in OPERA emulsion part in details. The last effect on emulsion is fog, which are the accidentally developed grains. It is an important background for emulsions and sometimes has severe effects. It will be discussed in next section.

4.2 The OPERA Emulsions

The OPERA is the first experiment that uses a large area of nuclear emulsions which is about 110,000 m^2. Therefore, it was impossible to produce them with the previous emulsion pouring techniques. Fuji Company in Japan established an automatic production set up and all the emulsion films were produced in the commercial film production lines. There were two important difficulties in the production of the OPERA emulsion films. The first one was the density of the gel and the other one was the thickness of the emulsion[37].

In the previous emulsion films, 50% of the total layer volume were filled by micro-crystals. But for the machine coating in the commercial production lines this value had to be decreased to 30%. This decrease in micro-crystal occupancy in emulsion brought an important problem to low tracking efficiency. When the AgBr viscosity decreases to 30%, the grain density, an important parameter which tells the number of grains in 100μm, decreases to 40%[37]. The solution was found by improving the sensitivity of the gel. As a result, while the volume occupancy degreased to 30%, which is important for the machine coating, the grain density was managed to be kept in the same level.

The second difficulty, thickness of emulsion, was the result of industrial production limitation. The required emulsion thickness was 50-100 μm whereas the photographic film is 10μm. So it was difficult to produce thick emulsions in the production lines for photographic films. In order to get the desired emulsion thickness, multi- coating method was applied. After the first layer was coated with 20μm emulsion, the second layer was coated on the first one. Therefore, by multi-coated technique, desired thickness of the emulsion was achieved. As a result of this automatic procedure, better thickness uniformity and better crystal diameter distribution have been obtained as seen in Figure 4.2.

There are two 42μm thick emulsion layers and between them there is 210μm thick plastics base as can be seen in Figure 4.3. A 1μm thick protection layer was put over the emulsion layers in order to protect them from outer effects. If there wouldn't be protection layers, un-

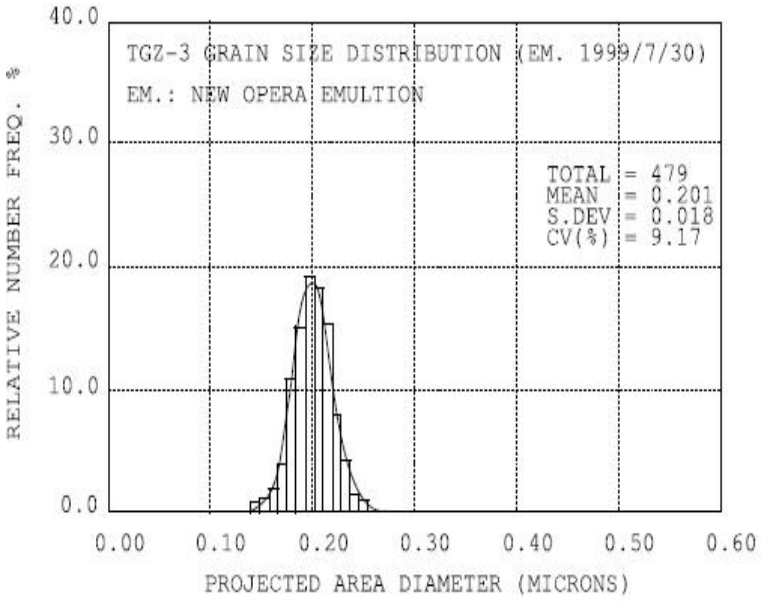

Figure 4.2: Distribution of crystal size of OPERA emulsions.

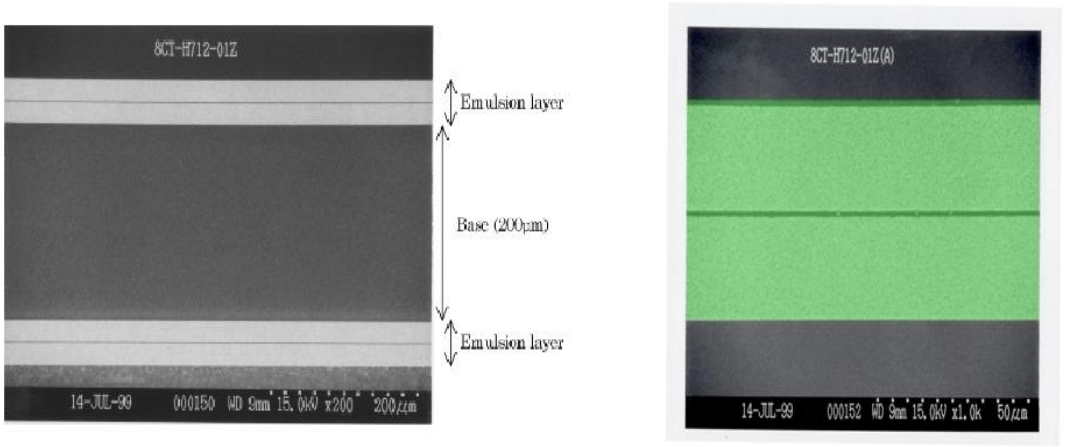

Figure 4.3: A microscopic view of the OPERA emulsion.

wanted black surface could be happened due to reaction with chemicals in the development process and due to direct interaction of emulsion with the lead plates inside the brick. Besides it's production properties, there is two factors that effect emulsion quality. The first one is the track density, which is the number of track grains per $100\mu m$. For the OPERA emulsion case the track density is measured to be $35 grains/100\mu m$. The second factor on the emulsion efficiency is the fog density, which is the number of accidentally developed grains in the $1000\mu m^3$ volume. For the case of OPERA emulsions this factor expected to be $< 8 grains/1000\mu m^3$. The main characteristics of the OPERA emulsion is given in Table 4.2

Table 4.2: Properties of the emulsions.

density	$\rho = 2.4 g/cm^3$
average atomic number	$< A >$=18.2
average atomic charge	$< Z >$ =8.9
radiation length	X_0 = 5.5 cm
$(\frac{dE}{dX})_{mip}$	1.55 MeV/g/cm^3 or 37keV/100μm
nuclear collision length	λ_T=33 cm

4.2.1 Defects in The OPERA Emulsion

Nuclear emulsions provides sub-micron resolution for tracking. Therefore, any small change in emulsion handling and processing may effect tracking efficiency. All process steps from production to the final use of emulsion in the detector must be tested carefully. There are three conditions that effect the tracking efficiency. Therefore, relevant corrections must be done at the reconstruction phase of tracking. These will be discussed in the next sections.

4.2.1.1 Shrinkage

During the development process, most of the AgBr crystals are washed out. Therefore the emulsion volume is decreased. Since the OPERA emulsion has 30% AgBr ratio in volume, shrinkage effect is lower then the hand made emulsions. Shrinkage has important effects on slope of the measured tracks. So in order to get the right values, tracking algorithms should consider the shrinkage effect. For the real slope of the track, measured micro-track slope should be corrected by shrinkage factor, which is the thickness of emulsion in the exposure

time divided by thickness of emulsion in the scanning time. That effect can be seen in Figure 4.4.

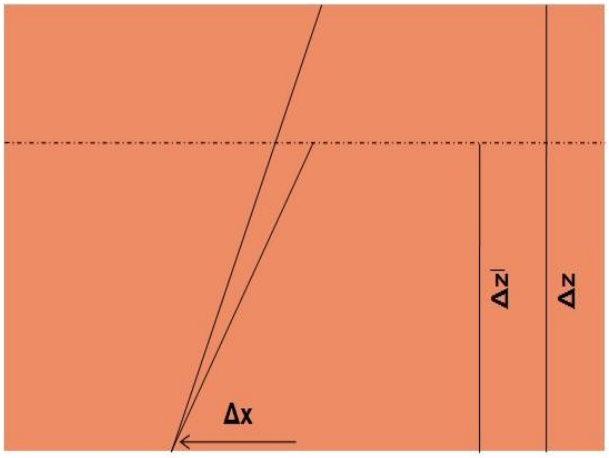

Figure 4.4: Schematic description of shrinkage effect.

4.2.1.2 Distortion

Distortion is a local deformation on the emulsion surface that is caused by the stress accumulated to the gelatin layer. Non-uniform drying or some mechanical effects cause distortion. Distortion has also side effects on the tracking efficiency. Due to the shift in grain position, it causes loss of efficiency for the base track reconstruction.

The distortion is measured as the angular difference between micro and base tracks as shown in Figure 4.5. We can define the distortion for both emulsion layers as;

$$\Delta\theta_{layer1} = \theta_1 - \theta_b \ \ (\ X\ and\ Y\ projection\ ), \tag{4.1}$$

$$\Delta\theta_{layer2} = \theta_2 - \theta_b \ \ (\ X\ and\ Y\ projection\ ). \tag{4.2}$$

For the hand made emulsion, distortion was an important problem which effects the tracking efficiency. But for the OPERA emulsion it is well understood and it is well controlled due to the automatical production techniques. An example of the typical distortion map of the OPERA emulsion can be seen in the Figure 4.6.

In 2006, a test exposure was performed at CERN with SPS beam. The brick was exposed to

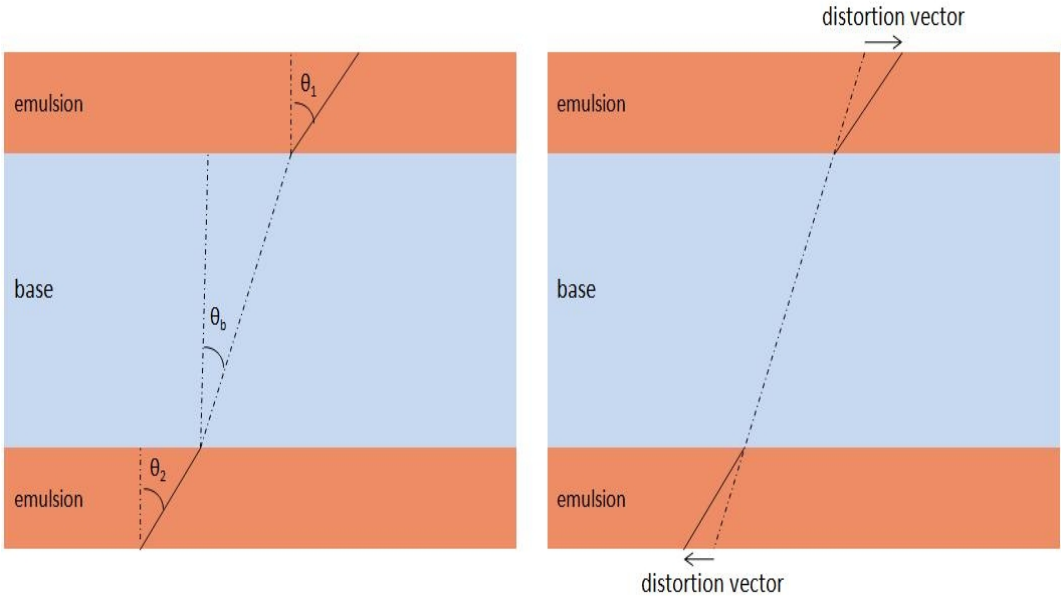

Figure 4.5: Schematic discription of the emulsion distortion.

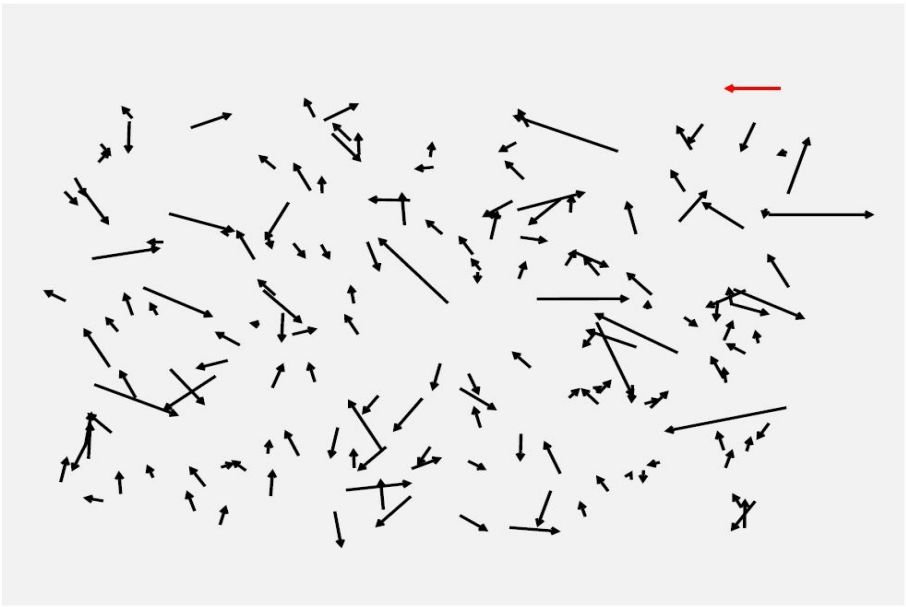

Figure 4.6: Typical distortion vector map of OPERA experiment.

muon and electron beams. After the exposure brick was scanned in Gran Sasso and shower analysis was performed [38]. This brick is also analyzed to check the quality of emulsion. The distortion maps of the first emulsion plate is shown in Figure 4.7 and in Figure 4.8. In

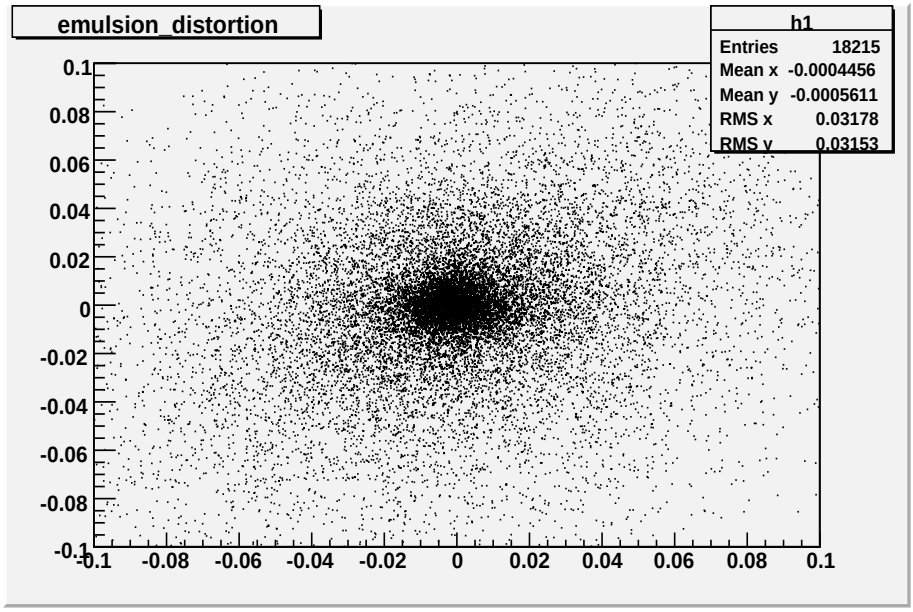

Figure 4.7: Distortion value in x-projection for both of the layers in the first emulsion of the OPERA brick.

order to study variations in distortion, 26 emulsion plates were scanned. In Figure. In Figure 4.9, the distortion values in x and y projections can be seen. We have observed that there is not a big variation in distortion values.

The average value of distortion is 3-3.5 mrad as shown in Figure 4.10. When it is compared with previous emulsion experiments, this distortion value is quite small. The smallness of the distortion in the OPERA emulsion is due to the machine production and well-controlled drying process applied by Fuji Company.

4.2.1.3 Fog Density

Fog is the black silver grain in the emulsion which is produced accidentally. There are some known effects that creates fog. One of them is the developing conditions. In Figure 4.11, the relation between fog density, grain density and developing time for the OPERA emulsion films can be seen. It is clear that 20^0C and 25 minutes are the most suitable conditions for developing process. It is known that some external effects like instantaneous change in

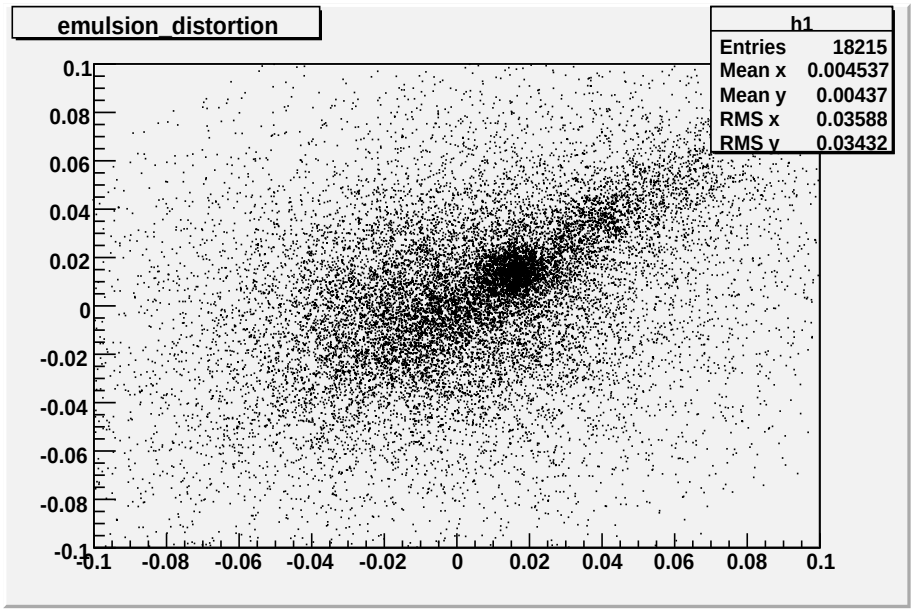

Figure 4.8: Distortion value in y-projection for both of the layers in the first emulsion of the OPERA brick.

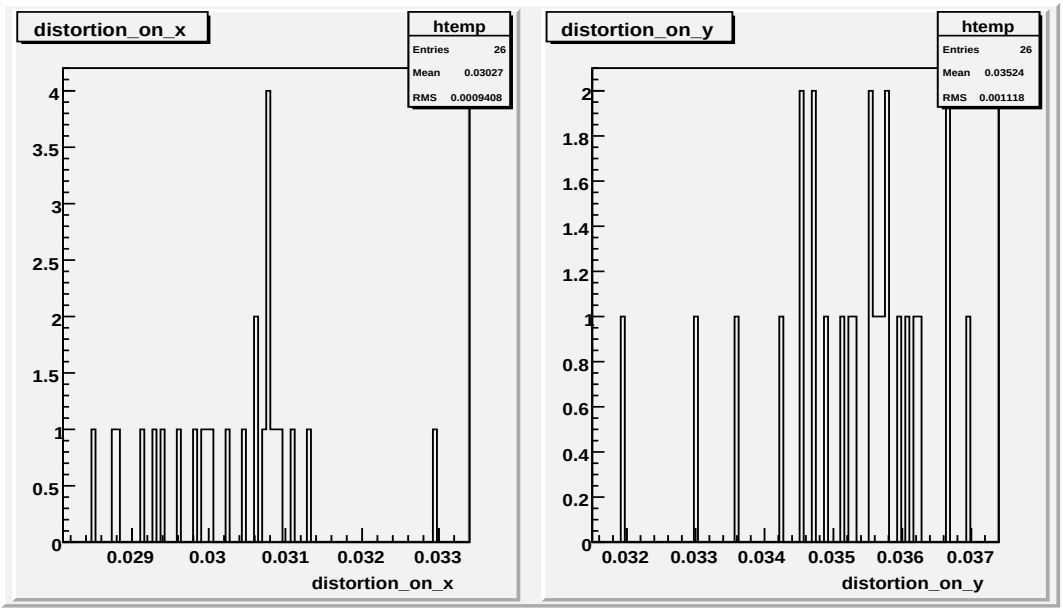

Figure 4.9: Distortion distributions of emulsion films in the brick in x and y projections.

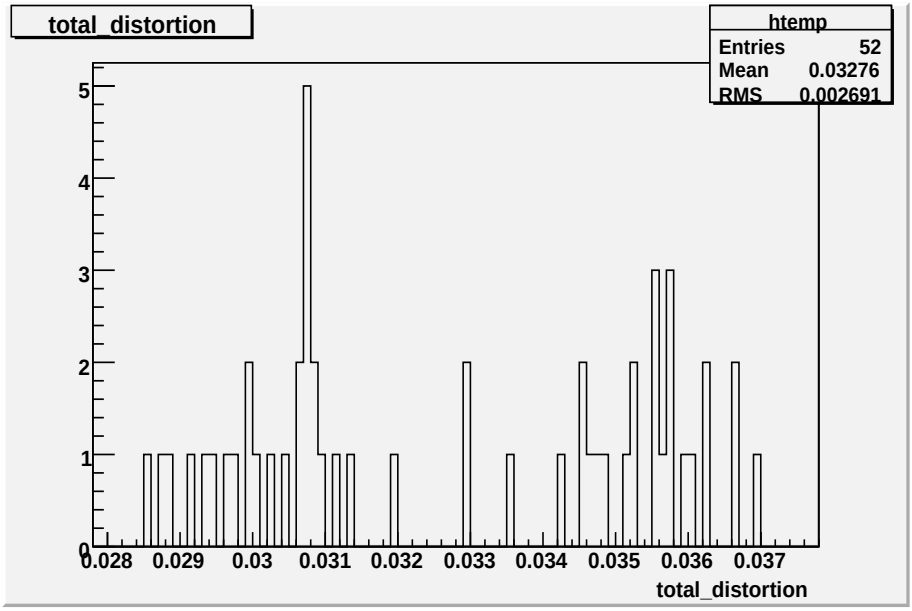

Figure 4.10: Mean value of OPERA emulsion distortion.

temperature or humidity, may also create fog.

There is no difference between the fog grain and grain that is created by the charged particle. A high fog density decreases the scanning speed and increases the number of fake tracks. Therefore, the density of the fog grains may effect the efficiency of tracking.

In OPERA, measurements on emulsions have showed that the fog density is lower then critical value, 12 grains/1000μm^3 for the brick emulsions [39]. The measurements are given in Table 4.3 and in Figure 4.12.

Table 4.3: Fog density measurements on some of the OPERA-October run ECC emulsions.

ID	FD (g/1000μm^3)
973	10.1± 0.2
1166	9.0± 0.2
1025	9.0± 0.2
635	9.2± 0.5
824	9.9± 0.3
1117	10.2± 0.3
605	8.8± 0.4
681	15.0± 0.5

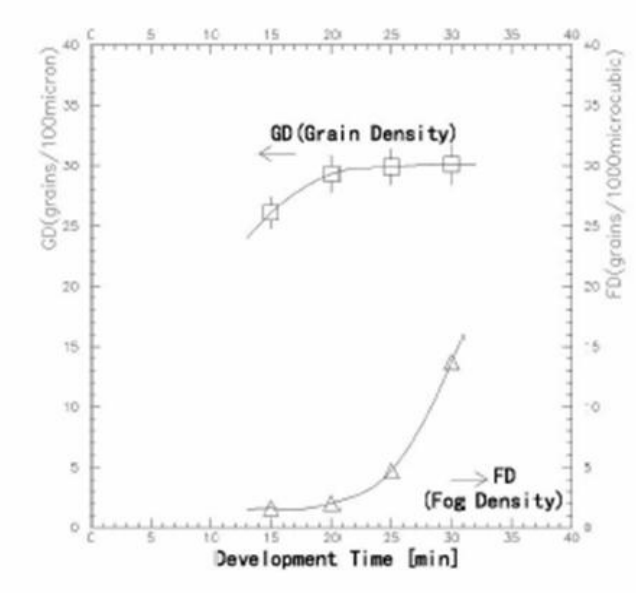

Figure 4.11: Fog density as a function of developing time.

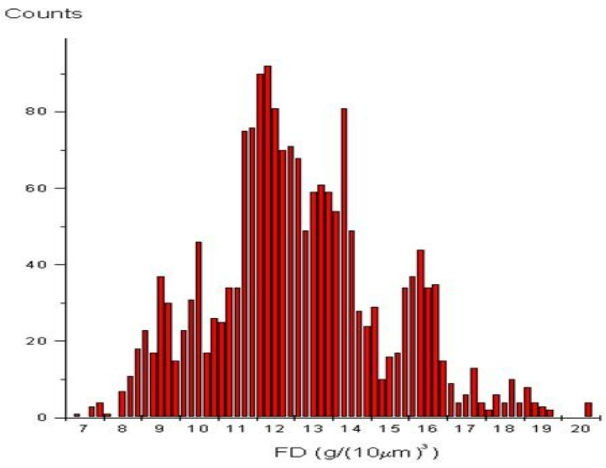

Figure 4.12: Fog density test results on the first shipment emulsions.

The fog density is more critical for Changeable Sheet scanning. This will be discussed in more details in Chapter 5.

4.2.1.4 Fading

As explained before, fading is the loss of latent image due to humidity and temperature conditions. For the OPERA emulsions, fading is not a problem. Since, as soon as the neutrino interaction takes place in the brick, it will be extracted from the detector and then developed. Moreover the temperature and humidity conditions of LNGS, are good enough to prevent from the fading.

4.3 The Scanning of The Emulsion Films

The read out of emulsion films have been done by means of microscope. The first automatic scanning system has been developed by Nagoya University and called as Track Selector [40]. Then scanning speed increased significantly and reached $2cm^2$/h. This microscope named as Ultra Track Selector (UTS) and was used in CHORUS and DONUT experiments [41].

In the OPERA experiment, the expected number of bricks to be extracted per day with the nominal intensity of the beam is about 30. This means that about 1000 emulsion films should be scanned. In order to fulfill this requirements, a scanning system at a speed of 20 cm^2/hour is needed. Based on R&D studies in Europe and Japan, two different scanning systems have been developed. In the following section these scanning systems will be described.

4.3.1 Nagoya Scanning System, S-UTS

The key features of the S-UTS shown in Figure 4.13, are the high speed camera with 3 kHz frame rate and a piezo-controlled displacement of the objective lens, synchronized to a continuous stage motion in order to avoid $go-stop$ of the microscope stage while taking images. The system uses Fast Programmable Gate Arrays (FPGAs), fast memory and a grabber board connected to the CCD camera 512×512 pixel.

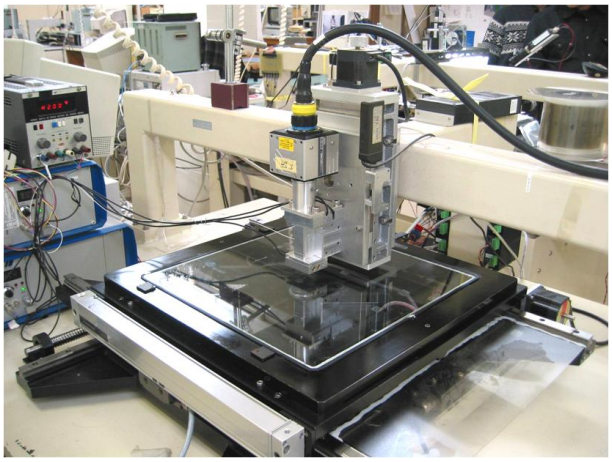

Figure 4.13: Picture of Nagoya scanning system, S-UTS.

4.3.2 European Scanning System-ESS

The development principles of ESS [42], are sub-micron precision, high tracking efficiency and low instrumental background. Unlike the Japanese S-UTS, ESS uses software based approach to the data processing. That allows easy and quick upgrade of the system.

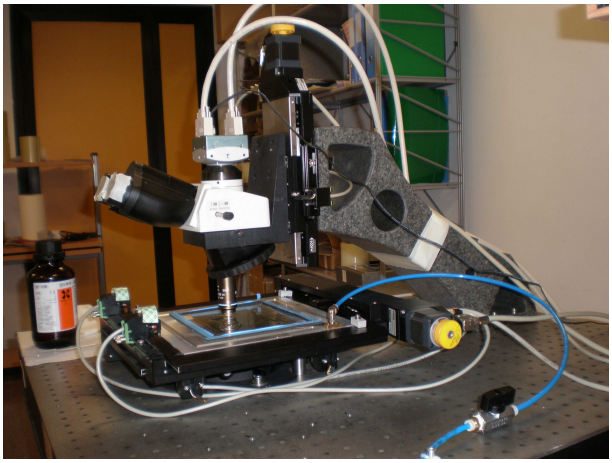

Figure 4.14: Picture of European Scanning System (ESS).

The ESS shown in Figure 4.14, has the following components and features,

- Support table which is vibration free and rigid that supports all the other components of the microscope.

- Scanning stage that is moving in X-Y position.
- Granite arm that supports the optical system and motor for moving in Z direction.
- Optics with large field of view ($360\times280\mu m^2$), 50X magnification and working distance 0.4 mm.
- Digital camera for image grabbing with 1280×1024 pixels and high frame rate that is mounted on the vertical stage and connected with a vision processor.
- An illumination system located below the scanning table.
- Powerful image processor.
- Software flexibility.

The working principle of the scanning system is that, by moving the optic, all the thickness of the emulsion is spanned. During that process digital images are taken in different depths/leyers of the emulsion, see Figure 4.15. The raw images are processed by using

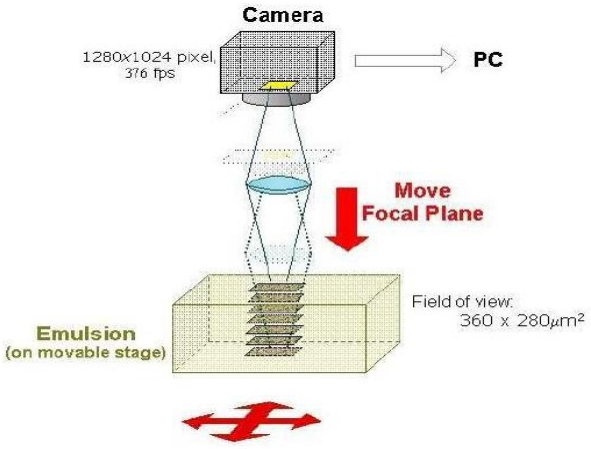

Figure 4.15: Working principle of ESS.

a high-pass digital filter to enhance the contrast between pixels that are images of focused grains and pixels darkened by not-in-focus grains or electronic noise. A threshold is applied to select the pixels that are candidates to become clusters. It is worth to distinguish between a grain, a physical object in the emulsion and a cluster, that is the digitized images of a grain.

After the position, area, angle information of the clusters are calculated, the next processing

step uses these information to recognize geometrical alignments between clusters of different layers. After alignment micro-tracks are generated in both of the emulsion layer.

Above described scanning and micro-track reconstruction processes are performed in real time during the scanning by the help of software. This software is developed by using object oriented C++ language. As a result of the scanning, raw data is created by the software. Raw data contain information related to the detected micro-tracks plus some general information related to the acquisition process.

As it was described, micro-track reconstruction is performed on-line. But the track reconstruction is an off-line process. In this process off-line reconstruction tool, FEDRA (Framework for Emulsion Data Reconstruction and Analysis) is used [43]. It is an object-oriented tool based on C++ language and developed in the ROOT [44] framework. By using FEDRA, $base - track$, connection of two micro-tracks that pass the plastic base and $volume - track$, that is formed by two or more base-tracks is formed. Therefore, all the tracks inside the brick are reconstructed and are analyzed.

CHAPTER 5

THE REFRESHING OF CHANGEABLE SHEETS(CS)

The CS is used as an interface between the electronic detectors and the ECC. The CS has two important roles in the experiment. The first one is to confirm the extracted brick which contains neutrino interaction and the second one is to save time for the emulsion scanning. The CS consists of two emulsion plates that are put in a laminated envelope. The emulsion films are the same as the ones used for the ECC brick. Since the background for the CS should be kept very low, a refreshing facility constructed in LNGS in order to erase the background tracks accumulated in the emulsion films during the transportation.

5.1 The Refreshing Facility

The refreshing facility was constructed in LNGS hole-B in the summer of 2005 in order to refresh CS for the OPERA experiment. A picture of the facility is shown in Figure 5.1. This work has been done in a collaboration between Japan, Russia and Turkey groups. The METU group, is one of the founders of refreshing facility and contributed this work from the beginning. The main steps of the process are the emulsion refreshing, packing, clinching and box loading. These steps will be described in details in the following sections.

5.1.1 Emulsion Refreshing

Nuclear emulsions are very sensitive to light and to the charged particles. Therefore any interaction with light or charged particles result tracks in the emulsion. Since the production of films was started in 2003, in time the background tracks were accumulated in the emulsion films. In particular, during the transportation emulsion films collected cosmic rays. But, the

Figure 5.1: CS Facility in INFN-LNGS Hole-B.

background tracks must be erased in order to improve tracking and reconstruction efficiency of the nuclear emulsion. A new method called refreshing[37] is applied to all emulsion films in order to erase these tracks. It consists of keeping the emulsion films at high relative humidity and high temperature. One can reach to 98 % efficiency of erasing the accumulated tracks while keeping a high sensitivity to the track reconstruction[37].

All emulsion films were refreshed in Tono mine in Japan before delivering to LNGS. Since transportation takes one month, emulsion films again integrate tracks from the cosmic ray flux. In particular, background track density is very critical for the CS since it acts as a trigger for the event location in the brick. Therefore, a second refreshing should be applied to CS films in LNGS.

Two refreshing chambers were reconstructed in CS barrack in LNGS-HoleB. They are made of stainless steel which have two main parts, see Figure 5.2. The first part is the place where emulsion films are put in. The second one is the humidifier part that changes humidity and the temperature conditions inside the chamber. The following reaction takes place in the refreshing process,

$$Ag_4 + O_2 + 2H_2O \rightarrow 4Ag^+ + 4OH^-. \tag{5.1}$$

The water in the reaction should be demineralized in order to avoid interactions of emulsion with impurities in normal water. By using the humidifier part, humidity and temperature inside the chamber can be adjusted. Then, Ag interacts with water molecules through reaction in Eqn. 5.1 and emulsion films are refreshed. There are four steps of emulsion refreshing

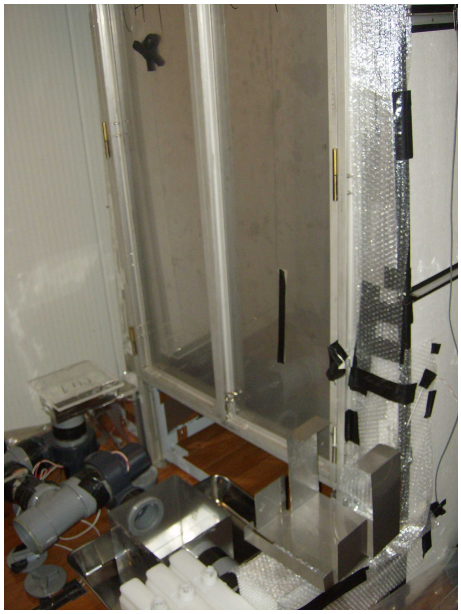

Figure 5.2: Refresh chamber in CS facility in Hole-B.

process. These will be explained below.

- Pre-Humidification:

  This is the starting mode of the refresh. In that mode humidifier is prepared for the process. Before starting to the refreshing process, all the components of humidifier are cleaned with alcohol. Then, two filters are placed inside the humidifier and it is closed. After adding the demineralized water to the humidifier, the refreshing process starts. This is indeed the first phase of the refreshing. Because of that, humidity is increased in order to prepare the emulsion films for the real refresh. In that mode humidity in the refreshing chambers should be $85\% - 90\%RH$ ($RelativeHumidity$), while the temperature is $23^0C - 25^0C$. This mode takes 1 day. During this mode air is circulated inside the chambers and the gas produced by the emulsion films are taken out by means of a fan.

- Humidification:

  This is the real mode for the emulsion refreshing. It is also called the "closed mode". In this mode the humidified air is circulated inside the chambers. Since the chambers are closed, humidity inside the chambers is increased to $98\% - 100\%RH$ at the temperature 25^0C-27^0C. This mode takes 3 days. During this mode, humidity and temperature

should be checked frequently. If RH is bigger then 100%, it cause the water drop on the emulsion films. On the other hand, lower RH and temperature inside the chamber result in low tracking efficiency. Therefore, there should be enough water in the humidifier. The reason why refreshing process takes three days can be understood from the Table 5.1. We can reach 98% erasing efficiency with 99% tracking efficiency in 3 days of refreshing.

Table 5.1: Erasing rate and tracking efficiency of emulsion refreshing at 98%-100% RH and at different durations.

Time	Tracking Efficiency [%]	Erasing Rate [%]
1 day	99	90
2 day	99	94
3 day	99	98

- Slow-drying

  In that mode refreshing is finished and films are let to dry. Humidifier must be opened in that mode and two filters must be removed. In this mode humidity inside the chamber decreases to $75\% - 85\% RH$. The slow-drying mode takes 1 day.

- Drying

  This is the final step of the refreshing process. In this mode, the humidifier is cleaned completely. Humidity inside the chambers decrease to $45\% - 50\%$ RH. The drying process takes 1 day. In Figure 5.3, the humidity and temperature graph can be seen for one full refreshing cycle. The four modes of the process are apparent.

One chamber has the capacity of 7000 emulsion films per one refresh process. Therefore, it is possible to refresh 14000 emulsions in one process which takes about one week. So far 365000 emulsion films have been refreshed successfully.

5.1.2 The Refreshing Efficiency

The important point about the refreshing is that we should preserve the original sensitivity of the films after refreshing. The emulsion film sensitivity after refreshing is measured in terms of grain and fog densities. Several tests were conducted to measure emulsion film sensitivity.

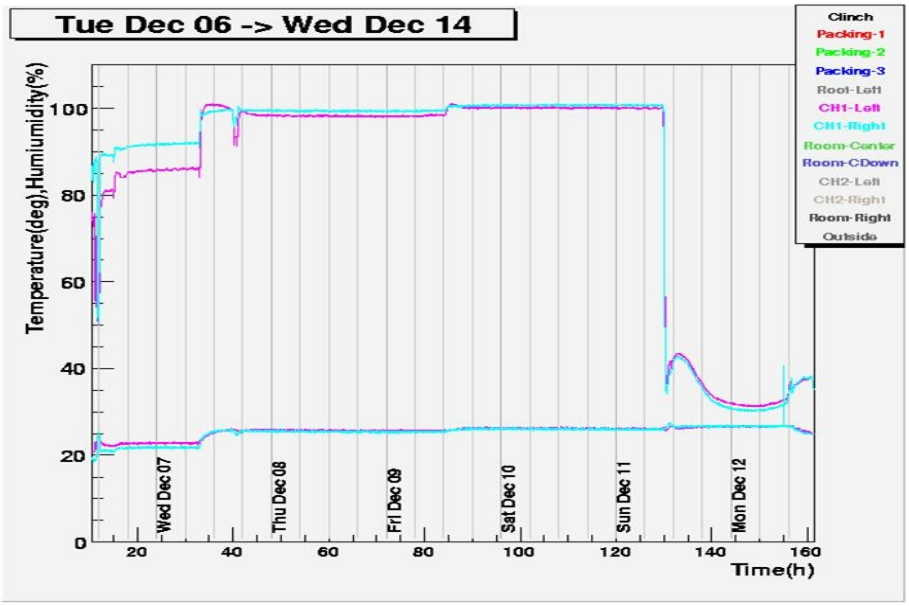

Figure 5.3: The humidity and temperature graph for emulsion refreshing.

The films were exposed to cosmic rays or to the test beams at CERN. Then, the grain and fog densities were measured. In order to have an efficient refreshing of the films, the grain density should be >30 grains/100μm, and the fog density should be <5 grains/1000μm^3.

We have performed a test exposure at CERN in July 2007. One brick was exposed to 20 GeV and 50 GeV muon and electron beams. After scanning of the emulsion films in Gran Sasso, we have measured the grain density and the fog density. They are within allowed range as seen in Table 5.2.

Therefore, based on our test, the refreshing process does not have any drawback on the emulsion sensitivity.

5.1.3 CS Film Packing

After refreshing, emulsion films are ready to be used in the experiment. Two refreshed films put together inside a polyethylene aluminium-laminated envelop. The air inside the envelope is taken out and the envelop is closed to fix emulsion position during the data taking. The packed emulsion films should be checked in case of any dust inside the envelope and misalignment of two emulsions film position. After packing, the packed emulsion doublet is

Table 5.2: Test Results of CERN-SPS Exposure on emulsion refresh efficiency in 4-11 July 2007

Refresh ID	Grain Density	Fog Density
061130-01D04	30.7 ± 1.2	3.7 ± 0.2
061130-02B06	30.4 ± 1.2	3.9 ± 0.2
061206-01A05	31.1 ± 1.3	4.3 ± 0.2
061207-02D08	30.8 ± 1.3	4.2 ± 0.2
070312-01D01	32.0 ± 1.3	3.9 ± 0.2
070313-02D01	31.0 ± 1.3	3.9 ± 0.2
070320-01B07	32.2 ± 1.3	4.1 ± 0.2
070322-02C06	31.6 ± 1.3	3.8 ± 0.2
070322-02D08	32.0 ± 1.3	4.3 ± 0.2
070328-01D03	32.1 ± 1.3	4.1 ± 0.2
070406-01D05	31.2 ± 1.2	4.8 ± 0.2
070608-01D05	31.3 ± 1.3	4.2 ± 0.2
070614-01D02	29.7 ± 1.2	4.8 ± 0.2
070614-02B04	30.7 ± 1.2	3.7 ± 0.2
070614-02D01	29.6 ± 1.2	4.0 ± 0.2
070621-01B04	30.8 ± 1.2	4.2 ± 0.2
070621-02B04	30.5 ± 1.2	6.1 ± 0.3

clinched from its 3 sides in order to fit into plastic box. The last step of CS production is to place envelope into the plastic box which is attached to the brick surface as shown in Figure 5.4.

5.2 The CS Fog Problem

As it was described in Chapter 3, the fog density effects the efficiency of the tracking. Since the fog density is very important for emulsion scanning and analysis, it is continuously measured from the beginning of the refreshing process. In principle, the value of fog density should be $< 5 grains/1000\mu m^3$ and even after 5 years operation of the experiment it is expected to be $< 10 grains/1000\mu m^3$. But the measurements that were performed in refreshing facility showed that fog density increases much faster than the expected as shown in Figure 5.5. This fast increase in the fog density was an indication of an outer effect like chemicals or some materials which accelerates this increase. Then the CS production steps and materials were checked carefully. Measurements were done on the laminated envelope at different conditions [45]. The test results are given in Table 5.3 and in Table 5.4

Figure 5.4: CS production steps, packing, clinching and installing. Finally CS is attached to the brick (ECC).

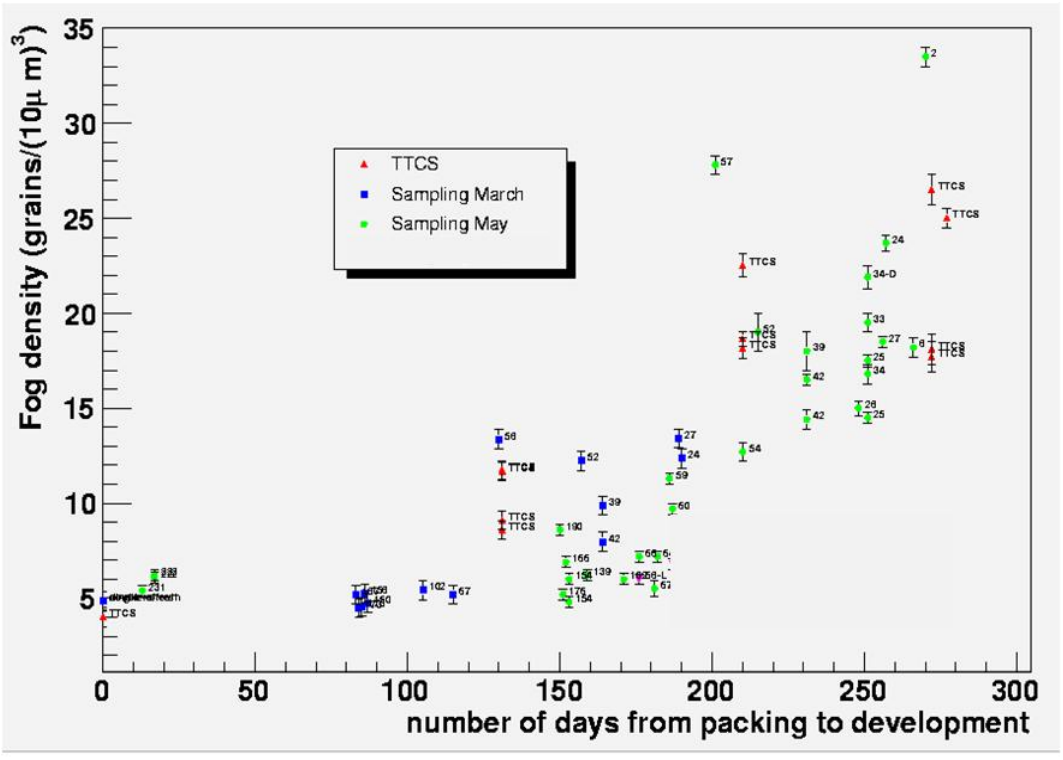

Figure 5.5: Fog density of CS films as a function of number of days from packing to development. It is clear that, some samples have very high fog density.

Table 5.3: Envelopes kept in ovens for different temperature and humidity conditions for 3 weeks. 3 weeks in oven is equivalent to 2 years time period.

	20^0C		35^0C	
	40%	50%	40%	50%
New Paper	5.8±0.1	5.8±0.3	7.5±0.1	6.3±0.1
Old Paper	3.8±0.1	3.9±0.3	4.2±0.1	4.0±0.1

Table 5.4: Envelopes kept in ovens for different temperature and humidity conditions for 8 weeks. 8 weeks in oven is equivalent to 5 years time period.

	20^0C		35^0C	
	40%	50%	40%	50%
New Paper	10.8±0.5	9.8±0.3	24.0±1	32±1
Old Paper	9.2±0.4	8.9±0.4	20.3±0.8	25±0.8

It is apparent that new laminated envelope has a side effect on the emulsion films. It causes to increase of the fog density. The components of the envelope film can be seen in the Table 5.5.

Table 5.5: The content of laminated film that is used to produce CS envelope.

Material	Role	Conventional	CS Type
Nylon	mechanical strength	15 μm	15 μm
Anchor coat	bonding	$< 1\mu m$	$< 1\mu m$
Polyethylene	bonding	13 μm	13 μm
Aluminium	light shielding	7 μm	7 μm
Anchor coat	bonding	$< 1\mu m$	$< 1\mu m$
Polyethylene	bonding	13 μm	13 μm
Black Polyethylene	light absorption	80 μm	35 μm
total		128 μm	83 μm

It was clarified that Anchor coat produces hydrogen gas in the envelope and this gas causes to increase the number of fogs in CS. Since the CS envelope is vacuum-packed, the hydrogen gas can not leak outside. As a result, hydrogen gas increases the fog density rapidly.

As a solution to this problem, small hole at the corner of the envelope was opened in order to release hydrogen gas as shown in Figure 5.6. Then, a vacuumed-packed emulsion films are compared with films with a hole. A comparison of the fog density is shown in Figure 5.7. It is clear that the sample with a hole on the envelope has low fog density as shown in Figure

5.8.

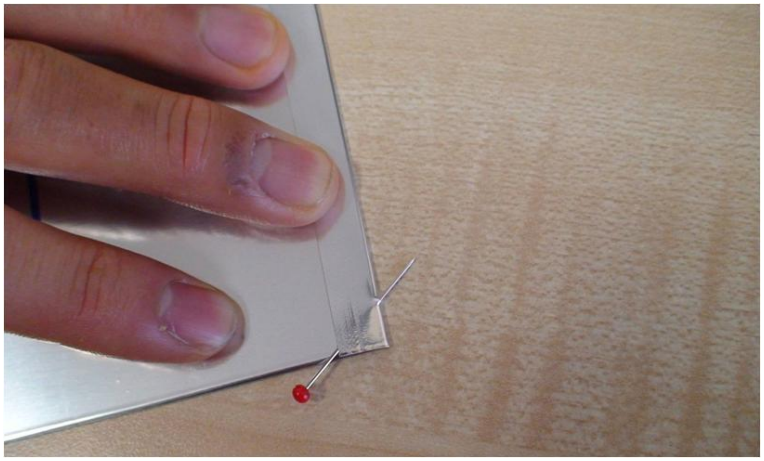

Figure 5.6: Picture of making a small hole at the corner of the CS envelope in order to release hydrogen gas.

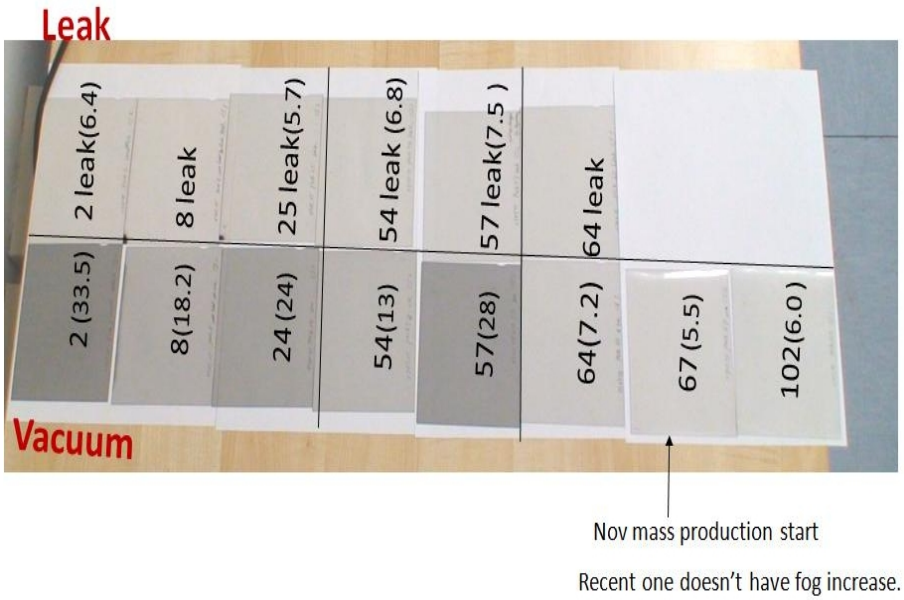

Figure 5.7: Picture of same ID CS envelope with hole or without hole. The difference in the fog density is even clear without microscopic measurement.

Based on these studies on the CS envelope, a small hole was opened at the corner of the all new CS envelope in order to release the hydrogen gas. The CS envelopes belonging to the old production will be replaced with the new ones which have a hole. This will be done in March-April 2009.

CHAPTER 6

D^0 BACKGROUND TO $\nu_\mu \rightarrow \nu_\tau$ OSCILLATIONS

6.1 Charm Production In OPERA Experiment

In the OPERA experiment, charmed particles are produced in CC neutrino interactions through the reaction

$$\nu_\mu N \rightarrow c\mu X \, . \tag{6.1}$$

The charmed particles have similar lifetimes and masses with the τ lepton. Therefore the charmed particles may constitute a background to oscillation signal if the primary muon is not identified. The background due to the charged charm was estimated in the experiment and shown in Table 6.1.

Table 6.1: Expected charm background for the different channels and for the different charmed hadrons. The values are normalized to 10^6 events.

	$\tau \rightarrow e$	$\tau \rightarrow \mu$	$\tau \rightarrow h$	total
Long D^+	4.3	0.7	2.7	7.7
Long D_s^+	2.6	0.4	4.1	7.1
Long Λ_c^+	0.1	0.3	0.2	0.6
Long total	7.0	1.4	7.0	15.4
Short D^+	0.4	-	0.3	0.4
Short D_s^+	0.5	-	0.8	0.5
Short Λ_c^+	0.2	-	0.2	0.2
Short total	1.1	-	1.3	1.1
Total	8.1	1.4	7.0	16.5

On the other hand neutral charm particles with 2-prong decay topology is also background to the short decay of τ lepton decaying into single hadron if the primary muon and one of the charged daughter particles is not identified in the event. This background topology is shown

in Figure 6.1. The estimation of this background is the subject of this thesis.

The charmed particle production rate in neutrino-nucleon interactions has been measured in the CHORUS experiment as [52],

$$\frac{\sigma(Charm)}{\sigma(CC)} = (5.9 \pm 0.4)\%, \tag{6.2}$$

$$\frac{\sigma(D^0)}{\sigma(CC)} = (2.67 \pm 0.18)\%. \tag{6.3}$$

By convoluting the charmed particle production rate with the OPERA neutrino spectrum, one gets production rates in OPERA,

$$\frac{\sigma(Charm)}{\sigma(CC)} = (4.28 \pm 0.25)\%, \tag{6.4}$$

$$\frac{\sigma(D^0)}{\sigma(CC)} = (1.75 \pm 0.14)\% \ . \tag{6.5}$$

The charmed hadron fractions are given in Table 6.2. The neutral charmed hadron fraction is 0.45. The two prong hadronic background ratio of D^0 is 0.54 as shown in Table 6.2. Therefore, the number of expected D^0 events decaying into two charged hadrons will be 175±17 for five years run of the OPERA experiment.

Table 6.2: Charm particles production ratio.

	Charm Particles Production Ratio
Λ_c^+	0.26
D^+	0.10
D_s^+	0.18
D^0	0.45

Table 6.3: D^0 decay modes with branching ratios.

Decay Mode	BR %
$D^0 \rightarrow \ fully\ neutrals$	21.08 ± 4.9
$D^0 \rightarrow \ \mu^+ h^-$	5.4 ± 1.3
$D^0 \rightarrow \ e^+ h^-$	5.4 ± 1.3
$D^0 \rightarrow \ h^+ h^-$	53.9 ± 4.5
$D^0 \rightarrow \ 2h^+ 2h^-$	13.4 ± 0.6

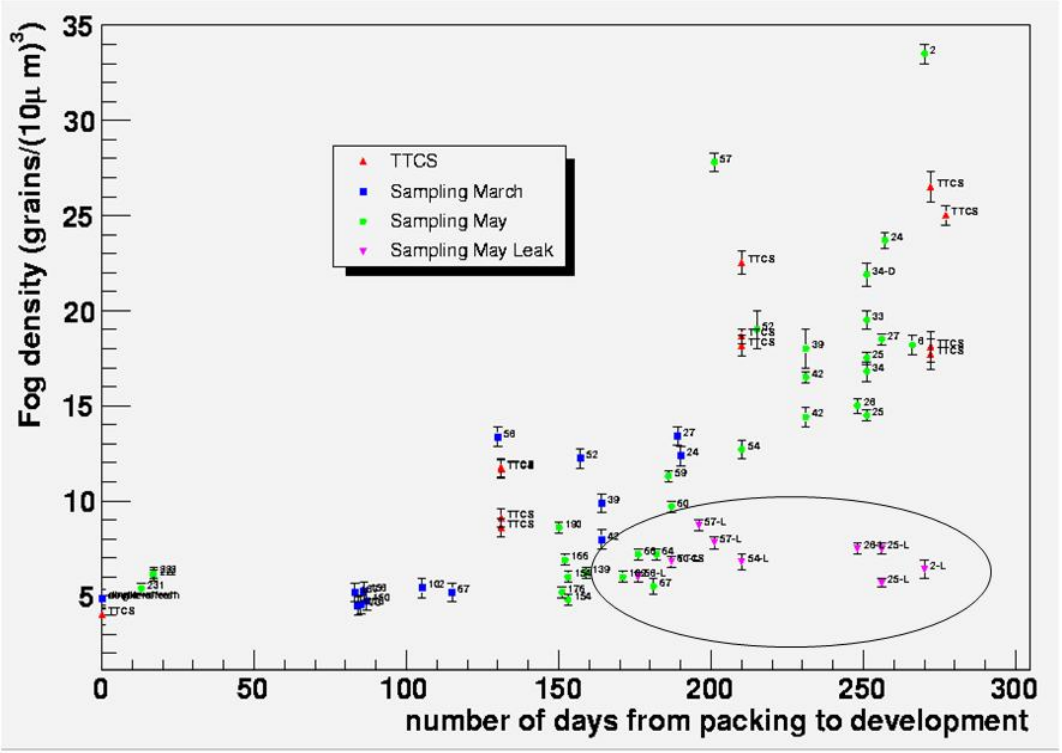

Figure 5.8: Fog density of the CS films with hole and without hole on the envelope. The circled ones corresponds to the sample with hole on the envelope.

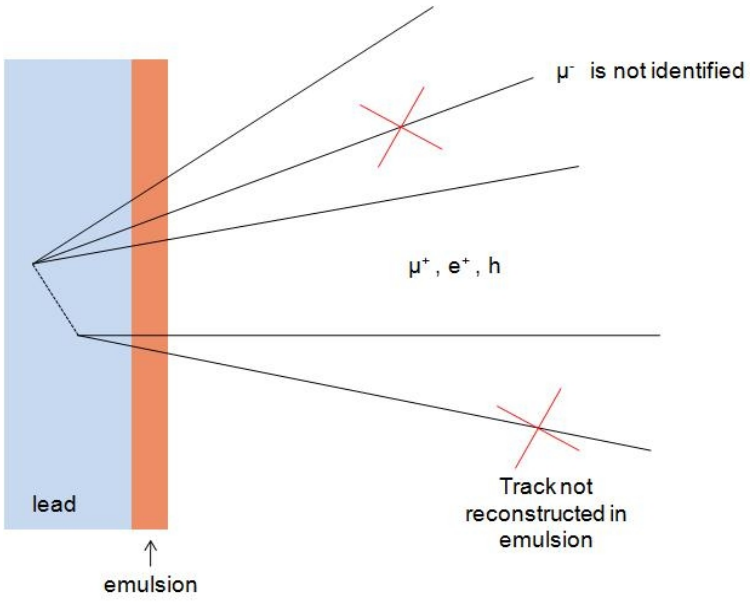

Figure 6.1: Schematic view of short decay of D^0 into 2-prong.

6.2 MC Simulation

The procedure of Monte Carlo simulation in the OPERA experiment consists of the generation of the physical events, the simulation of the detector response and reconstruction. A software framework called as OpRelease has been developed for the Monte Carlo simulation of the experiment[46]. OpRelease consists of packages which were written in object-oriented language C++. These packages were integrated by using CMT tool [47].

As an event generator NEGN[48] which was developed in the NOMAD[49] experiment has been used. It produces an ascii file with generator events information which is used as an input to OpRoot package. OpRoot performs the detector simulation and is based on GEANT3[50]. The output of OpRoot is a ROOT tree containing hit information.

In order to reconstruct base and volume tracks, ORFEO package has been used. In the ORFEO[51] package following steps were performed,

- position and slope smearing
- cluster size simulation
- efficiency micro-track creation
- plate to plate affine transformation and linking.

After these steps, the reconstructed MC data is analyzed with ROOT.

6.3 Estimation of D^0 Background

Using OpRoot and ORFEO packages, 9000 charm events have been produced. The composition of the charm events in the MC data is given in Table 6.4. In order to analyze the MC data, a code in C language was written.

The flight length of D^0 is calculated as

$$FlightLength = \sqrt{(x_1 - x_2)^2 + (y_1 - y_2)^2 + (z_1 - z_2)^2}, \tag{6.6}$$

Table 6.4: The composition of charm events in MC data.

	Charm Particles Production Ratio
Λ_c^+	1695
D^-	2116
D_s^+	520
D^0	4364

where (x_1, y_1, z_1) is the position of neutrino interaction vertex and (x_2, y_2, z_2) is the position of decay vertex. The flight length distribution of D^0 according to Eqn. 6.6 is given in Figure 6.2.

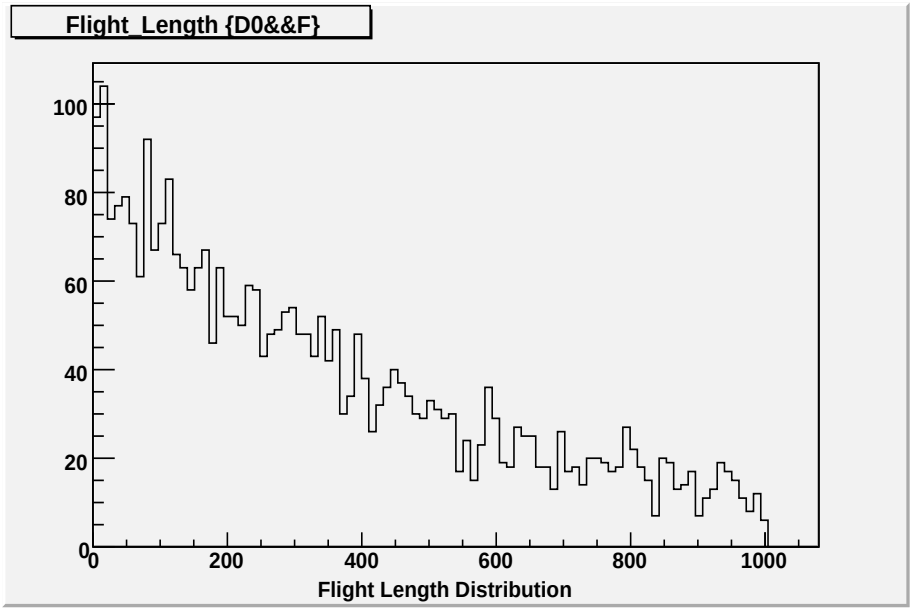

Figure 6.2: D^0 flight length distribution.

Due to the inefficiency of emulsion scanning and reconstruction program, not all particle tracks can be reconstructed. In order to find reconstructed tracks, a track matching algorithm is applied. The true track slopes are compared with the reconstructed ones. Then, the track is flagged as reconstructed if the angular residual between reconstructed and true track is less than 30mrad.

The event will constitute a background to the τ decay if one of the daughters of D^0 is not reconstructed. The efficiency of track reconstruction is 76%. The number of events with one

reconstructed daughter track is found to be 471. Therefore, the probability of reconstruction of one daughter is 24%. Then the number of D^0 background to the τ lepton can be written as

$$D^0_{bg} = N_{D^0} \times \varepsilon_{short} \times \varepsilon_{1-prong} \times \varepsilon_{\mu miss} \times \varepsilon_{selection} \times \varepsilon_{loc} \quad (6.7)$$

where

- N_{D^0} is the number of expected D^0 events decaying into 2-prong for five years of data taking. It is estimated to be 175±17 events.
- ε_{short} is the ratio of short 2-prong decay to all 2-prong events and found to be 0.54.
- $\varepsilon_{1-prong}$ is the ratio of 2-prong events with one reconstructed daughter track. This is found to be 0.24.
- $\varepsilon_{\mu miss}$ is the primary muon misidentification efficiency which was estimated to be 10%.
- $\varepsilon_{selection}$ is the selection efficiency of D^0 short events. We require the flight length $> 50\mu m$ and kink angle $> 20mrad$. Based on the MC simulation, this efficiency is found to be 77%.
- ε_{loc} is the location efficiency of ν_μCC events. This efficiency was estimated as 80% in previous MC simulation.

When all of these efficiencies inserted to the background formula, we obtain,

$$D^0_{background} = 175 \times 0.54 \times 0.24 \times 0.10 \times 0.77 \times 0.80 = 1.40 \pm 0.02 \quad (6.8)$$

It is possible to reduce this background by applying transverse momentum (p_t) cut. Transverse momentum of the daughter particle is defined as,

$$p_t = p \times \theta_{kink} , \quad (6.9)$$

where θ_{kink} is the kink angle and p is the true momentum of daughter track. The kink angle and momentum distribution can be seen in In Figure 6.3 and in Figure 6.4. We applied two different p_t cuts: one is p_t >250MeV and the other is p_t >450MeV. The efficiency of

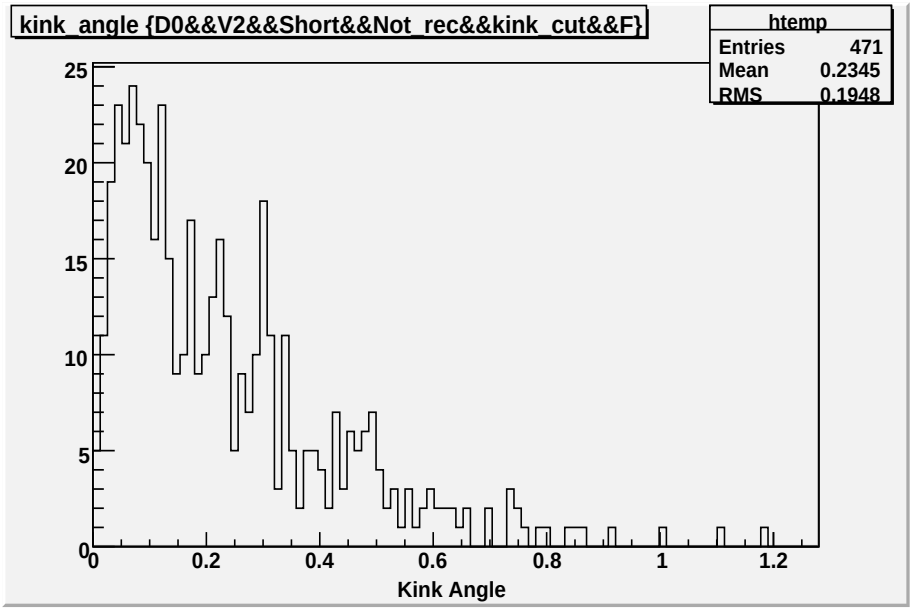

Figure 6.3: Kink angle distribution of background events.

p_t >250MeV cut is calculated to be 64%. Then after this cut, the number of D^0 background becomes,

$$D^0_{background} = 1.40 \pm 0.02 \times 0.64 = 0.90 \pm 0.01 \; events. \tag{6.10}$$

As a harder cut we require p_t >450 MeV based on p_t distribution in Figure 6.5. This cut reduce number of background events to

$$D^0_{background} = 1.40 \pm 0.02 \times 0.29 = 0.40 \pm 0.005 \; events. \tag{6.11}$$

Based on the our estimation, D^0 background to $\nu_\mu \rightarrow \nu_\tau$ oscillation is not negligible. It is close to the total background to the oscillation signal.

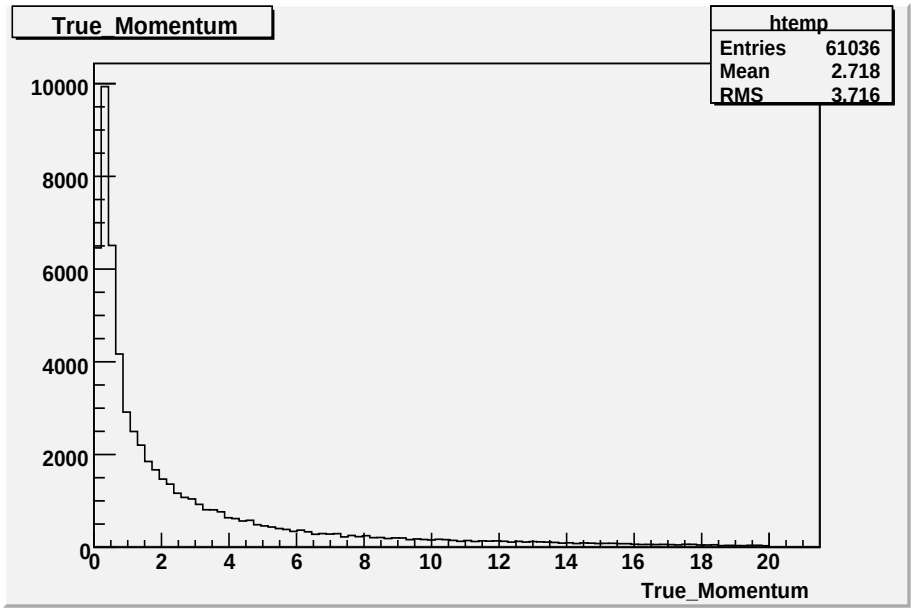

Figure 6.4: Momentum distribution of the true tracks.

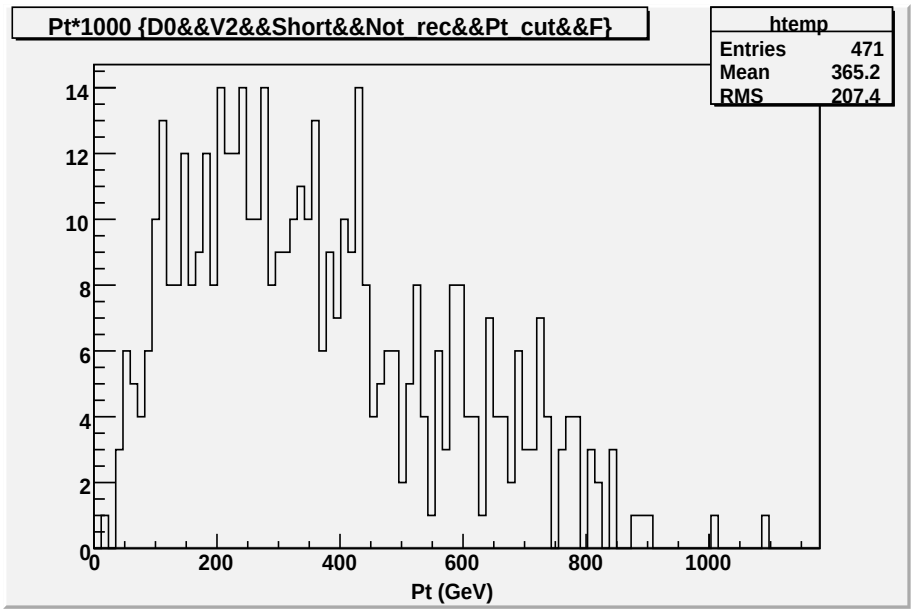

Figure 6.5: p_t distribution for the possible background events. Right graph is in GeV range and left graph is in MeV range.

CHAPTER 7

CONCLUSIONS

The OPERA experiment aims to prove $\nu_\mu \rightarrow \nu_\tau$ oscillation via direct observation of ν_τ CC interactions. The detector was completed in 2008. The physics run with the full target took place in 2008 and an integrated luminosity of 1.79×10^{19} pot was accumulated. During this run 10100 events correlated in time with the beam. In total 1700 events were triggered in the OPERA detector.

The main sub-detector in OPERA is ECC which acts as a target for neutrino interactions and simultaneously as a detector for the measurement of electron shower and charged particle momentum. In order to improve ECC performance the emulsion films were refreshed in Japan before shipping to Italy. The efficiency of this process is measured to be 98%. On the other hand, an emulsion film doublet is attached to behind each brick in order to confirm and locate the tracks produced in neutrino interaction. The use of CS doublet is very beneficial to avoid useless emulsion scanning and the film handling. In order to have the required performance of the CS doublet, the background level in the CS must be extremely low. Since emulsion films accumulate additional cosmic rays during 1 month transportation from Japan to Italy, this background effects CS performance and must be reduced to very low level like $10^{-3} tracks/cm^2$. In order to reduce the background track density, a second refreshing must be performed at LNGS. Therefore, a refreshing facility was constructed in LNGS and 365000 emulsions were refreshed. We have performed tests to measure efficiency of refreshing process and sensitivity of emulsion films after refreshing. Based on these measurements we have verified that, the background tracks in CS films erased without decreasing the film sensitivity.

In oscillation experiments, a significant background comes from the production and decay of charged particles. This is also case for the OPERA experiment. However, thanks to sub-

micron resolution of nuclear emulsion this background is estimated to be less than one event [9]. But this estimation was done by considering only charged charm. On the other hand, neutral charm decays also constitute a background to decay of τ lepton. Since the decay takes place in the brick, we can not identify whether charm particle is neutral or charged. Only way to distinguish neutral charm and charged charm is to measure the number of charged daughter particles. In the case of charged charm decay, number of the charged daughter must be an odd number but it must be even in neutral charm decay. If the reconstruction algorithm and emulsion scanning were perfect we could identify the neutral and charged charm decays with 100% efficiency, and neutral charm events would not be a background to τ decay. Since no detector is perfect, there are inefficiencies in the reconstruction of the charged daughter particle in the OPERA detector. Therefore, a neutral charm decay topology can be reconstructed as decay topology which mimics the τ lepton decay. The estimation of this background is the subject of this thesis. We have shown that background due to production and decay of neutral charmed particles is not negligible to $\nu_\mu \rightarrow \nu_\tau$ oscillation. This background can be reduced by considering reconstructed micro-tracks or base tracks, and applying additional cuts.

REFERENCES

[1] W.Pauli, letter to a physicist's gathering at Tubingen,December 4,1930.Reprinted in *Wolfgang Pauli,Collected ScientificPapers*,ed.R.Kronig and V.Weisskopf, Vol.2 , p.1313,New York,1964.

[2] C. L. Cowan, F. Reinas, F. B. Harrison, H. W. Krause and A. D. Guire, *Detection of free neutrino : A Conformation*, Science 124, 103(1956).

[3] G.Danby *et al*, Phys. Rew. Lett. 9 (1962) 36.

[4] M. L. Perl et al, "Evidence for Anomalous Lepton Production in e+e- Annihilation" Phys. Rev. Lett., 35, 1489 (1975)

[5] K.Kodama *et al*, Phys. Lett. B504 (2001) 218.

[6] C. Kraus *et al*, hep-ex/0412056 (2004) .

[7] K. Assamagan *et al*, Phys. Rev. D53 (1996) 6065.

[8] R. Barate *et al*, Eur. Phys. J. C2 (1998) 395.

[9] OPERA Collaboration, M.Guler *et al*, *Experimental Proposel*, CERN-SPSC-2000-028.

[10] The Homestake Collaboration, R. Davis, D. S. Harmer and K. C. Hoffman, Phys. Rew. Lett. 20 (1968) 1205.

[11] The Homestake Collaboration, R. Davis, Prog. Part. Nucl. Phys. 32 (1994) 13.

[12] The GALLEX Collaboration, P. Anselmann *et al.*, Phys. Lett. B285 (1992) 376.
W. Hampel *et al.*, Phys. Lett. 388 (1996) 384.
W. Hampel *et al.*, Phys. Lett. 347 (1999) 127.

[13] E. Bellotti, Proc. of TAUP 2003, University of Washington, Seattle, Washington.

[14] J. N. Abdurashitov *et al.*, J. Exp. Theor. Phys. 95 (2002) 181.

[15] Kamiokande Collaboration, K. S. Hirata *et al.*, Phys. Rev. D 38 (1988) 448.
K. S. Hirata *et al.*, Phys. Rev. D 38 (1991) 2241.
K. S. Hirata *et al.*, Phys. Rev. Lett. 77 (1996) 1683.

[16] Super-Kamiokande Collaboration, S. Fukuda *et al.*, Phys. Rev. Lett. 86 (2001) 5651.
S. Fukuda *et al.*, Phys. Rev. Lett. 86 (2001) 5656.

[17] Super-Kamiokande Collaboration, Y.Fukuda *et al*, Phys. Rev. Lett. 81 (1998) 1562.

[18] The SNO Collaboration, A. Hallin *et al.*, Nucl. Phys. A 663 (2000) 787.

[19] The MACRO Collaboration, M. Ambrosio *et al*., Phys. Lett. B 434 (1998) 451; M. Ambrosio *et al*., Eur. Phys. J. C36 (2004) 323.

[20] Super-Kamiokande Collaboration, Y. Fukuda *et al*., Phys. Rev. Lett. 81 (1998) 1562; Y. Ashie *et al*., hep-ex/0501064 (2005) (Submitted to Phys. Rev. D).

[21] Soudan2 Collaboration, W. W. Allison *et al*, Phys. Lett. B499 (1999) 137; M.Sanchez *at al*, Phys. Rev. D68 (2003) 11304.

[22] K2K Collaboration, Phys. Rev. D74 (2006) 072003.

[23] K2K collaboration, Phys. Rev. Lett. 90 (2003) 041801 (hep-ex/0212007).

K2K collaboration, Phys. Rev. Lett. 94 (2005) 081802 (hep-ex/0411038).

[24] MINOS Collaboration, arXiv:hep-ex/0605058 v2 (2006).

[25] R.N. Mohapatra and P.B. Pal, Massive Neutinos in Physics and Astrophysics, River Edge, N.J. World Scientific 2004.

[26] M. Goldhaber, L. Grodzins, A. W. Sunyar, Phys. Rev. 109, 1015 - 1017 (1958).

[27] G. Acquistapece *et al*.,"The CERN neutrino beam to Gran Sasso (NGS)", Conceptual Technical Design, CERN 98-02 and INFN/AE-98/05 (1998).

[28] S.Eidelman *et al*., Phys. Lett. B592 (2004).

[29] Natalia DiMarco, Scanning meeting, 29/10/2008, LNGS- Italy.

[30] C.Lattes, H.Muirhead, G.Occhialini, C.Powell, *Processing involving charged mesons*, *Nature* 159 (1947) 694.

[31] D. Allasia *et al*., Nucl. Phys. B176 (1980) 13.

[32] S. Aoki *et al*., Nucl. Instr. Meth. A274 (1989) 64.

[33] Ushida *et al*., Phys.Rev.Lett. 1981, 47,24.

[34] Ushida, N. *et* al., Phys. Rev. Lett. 56 (1986) 1767-1770.

Ushida, N. *et* al., Phys. Rev. Lett. 56 (1986) 1771-1774.

Ushida, N. *et* al., Phys. Rev. Lett. 51 (1983) 2362-2365.

[35] CHORUS Collaboration, NIM, A 401 (1997), 7-44.

[36] K. Kodoma, *et al*., Phys. Lett. B504 (2001) 218.

[37] T. Nakamura et al., Nucl. Instrum. Meth. A 556, 80 (2006).

[38] M. Fatih Bay, MS thesis, METU, 2008.

[39] Chiara Sirignano, OPERA Collaboration Meeting, Maiori-Italy, 05/06/2007.

[40] S. Aoki, *et al*., Nucl. Instr. Meth. B 51 (1990) 466.

[41] K. Kodoma, *et al*., Phys. Lett. B 504 (2001) 218-224.

[42] *N.D'Ambrosio*, Nucl. Instr. Meth. A477 (2002) 431; *N.D'Ambrosio*, Nucl. Instr. and Meth. A525 (2004) 193; G. Sirri, Automatic scanning of emulsion films for the OPERA experiment, Degree Thesis, University of Bologna (2005).

[43] V. Tioukov, *et* al. Framework for emulsion data reconstruction and analysis in the OPERA experiment., Nuclear Instruments and Methods in Physics Research A 559 (2006) 103105.

[44] ROOT-CERN web page, http://root.cern.ch, visited on June 4, 2008.

[45] Akitaka Ariga, OPERA Collaboration Meeting, Maiori-Italy, 01/06/2007.

[46] OpRelease web page, http://emulsion.na.infn.it/wiki/index.php/OpRelease, visited on June 4, June 2008.

[47] CMT web page, http://www.cmtsite.org/, visited on June 8, 2008.

[48] D. Auterio, Nucl. Phys. Proc. Suppl. 139 (2005) 253.

[49] NOMAD web page, http://nomad-info.web.cern.ch/nomad-info/, visited on June 9, 2008.

[50] GEANT we page, http://wwwasdoc.web.cern.ch/asdoc/geantold/GEANTMAIN.html, visited on June 15, 2008.

[51] ORFEO web page, http://emulsion.na.infn.it/wiki/index.php/ORFEO, visited on July 15, 2008.

[52] CHORUS collaboration, Phys.Lett.B613:105-117, (2005).

APPENDIX A

GENERAL FORMALISM OF NEUTRINO OSCILLATION

Assuming that neutrinos are massive and mixed, the neutrino flavor eigenstate $|\nu_\alpha\rangle$ can be expressed as a superposition of the mass eigenstates $|\nu_i\rangle$ with unitary matrix, U.

$$\nu_\alpha = \sum U_{\alpha i}\nu_i, \tag{A.1}$$

where

$$UU^\dagger = 1.$$

Let assume that neutrino mass differences are small and different neutrino masses can not be resolved in neutrino production and detection process. For the neutrino state with momentum $\vec{p}$ we have

$$|\nu_\alpha\rangle = \sum U^*_{\alpha i}|\nu_i\rangle. \tag{A.2}$$

Where $U^*_{\alpha i}$ is the transition matrix from ν_α to ν_i. Then the time evolution of this can be written as

$$|\nu_\alpha\rangle_t = \sum U^*_{\alpha i}e^{-iE_1 t}|\nu_i\rangle. \tag{A.3}$$

We can also write

$$|\nu_i\rangle = \sum U_{\alpha' i}|\nu_{\alpha'}\rangle, \tag{A.4}$$

where $U_{\alpha' i}$ is the transition matrix from ν_i to $\nu_{\alpha'}$ and time evolution of this as

$$|\nu_i\rangle_t = \sum U_{\alpha' i}e^{-iE_2 t}|\nu_{\alpha'}\rangle. \tag{A.5}$$

So if we combine Eqn.A3 and Eqn.A5 we get

$$|\nu_\alpha\rangle_t = \sum U^*_{\alpha i}e^{-iE_1 t}U_{\alpha' i}|\nu_{\alpha'}\rangle. \tag{A.6}$$

If we define $A_{\alpha'\alpha}$ which is transition amplitude as,

$$A_{\alpha'\alpha} = U^*_{\alpha i}e^{-iE_1 t}U_{\alpha' i}, \tag{A.7}$$

Eqn.A6 becomes

$$|\nu_\alpha\rangle_t = \sum A_{\alpha'\alpha}|\nu_{\alpha'}\rangle. \tag{A.8}$$

Now let's consider the probability to oscillate to another flavor $\nu_{\alpha'}$

$$|\langle\nu_{\alpha'}|\nu_\alpha\rangle|^2 = |\sum A_{\alpha\alpha'}|\nu_{\alpha'}\rangle\langle\nu_{\alpha'}|U_{\alpha' i}e^{iE_2 t}U^*_{\alpha i}|^2, \tag{A.9}$$

$$= |\sum U^*_{\alpha i}e^{-iE_1 t}U_{\alpha' i}U^*_{\alpha' i}e^{iE_2 t}U_{\alpha i}\langle\nu_{\alpha'}|\nu_{\alpha'}\rangle|^2, \tag{A.10}$$

where $\langle\nu_{\alpha'}|\nu_{\alpha'}\rangle = 1$ and $U_{\alpha' i}U^*_{\alpha' i} = 1$

$$= |\sum U^*_{\alpha i}e^{i(E_2-E_1)t}U_{\alpha' i}|^2, \tag{A.11}$$

if we add and subtract 1 we get

$$= |\sum U^*_{\alpha i}[(e^{i(E_2-E_1)t} - 1) + 1]U_{\alpha' i}|^2, \tag{A.12}$$

$$= |\delta_{\alpha\alpha'} + \sum U^*_{\alpha i}(e^{i(E_2-E_1)t} - 1)U_{\alpha' i}|^2. \tag{A.13}$$

Assuming the relativistic neutrino, we can write

$$E_j = \sqrt{p^2 + m_j^2} \simeq p + \frac{m_j^2}{2p}.$$

Besides if we define L which is the distance between the source and detection, $L \simeq t$ if we set c=1, since neutrinos move with a speed closer to the speed of light. As a result $(E_2 - E_1)t$ term becomes

$$(E_2 - E_1)t = \Delta m^2_{12}\frac{L}{2p}.$$

Using this, Eqn.A13 can be written as

$$|\langle\nu_{\alpha'}|\nu_\alpha\rangle|^2 = |\delta_{\alpha\alpha'} + \sum U^*_{\alpha i}U_{\alpha' i}(e^{-i\Delta m^2_{12}\frac{L}{2p}} - 1)|^2. \tag{A.14}$$

$$P(\nu_\alpha \to \nu_{\alpha'}) = |\delta_{\alpha\alpha'} + \sum U^*_{\alpha i}U_{\alpha' i}(e^{-i\Delta m^2_{12}\frac{L}{2p}} - 1)|^2, \tag{A.15}$$

where the Δm^2_{12} term stands for the mass square difference of ν_α and $\nu_{\alpha'}$.